



# Optimal transport and control of active drops

Suraj Shankar<sup>a,1</sup>, Vidya Raju<sup>b,1</sup>, and L. Mahadevan<sup>a,b,c,2</sup>

Edited by Daan Frenkel, University of Cambridge, Cambridge, United Kingdom; received December 7, 2021; accepted May 25, 2022

Understanding the complex patterns in space–time exhibited by active systems has been the subject of much interest in recent times. Complementing this forward problem is the inverse problem of controlling active matter. Here, we use optimal control theory to pose the problem of transporting a slender drop of an active fluid and determine the dynamical profile of the active stresses to move it with minimal viscous dissipation. By parametrizing the position and size of the drop using a low-order description based on lubrication theory, we uncover a natural “gather–move–spread” strategy that leads to an optimal bound on the maximum achievable displacement of the drop relative to its size. In the continuum setting, the competition between passive surface tension and active controls generates richer behavior with futile oscillations and complex drop morphologies that trade internal dissipation against the transport cost to select optimal strategies. Our work combines active hydrodynamics and optimal control in a tractable and interpretable framework and begins to pave the way for the spatiotemporal manipulation of active matter.

optimal transport | optimal control | active matter | droplet motion

In recent years, active fluids composed of internally driven units have emerged as a powerful platform to manipulate and morph matter far from equilibrium (1–3). Such fluids have been assembled from a variety of biological and synthetic constituents, including self-propelled colloids, driven biofilaments, and living cells (4–7). These systems often exhibit complex spatiotemporal dynamics and pattern formation that have been the focus of intense research efforts in the past two decades or so.

While a great deal is now understood about the emergent collective dynamics in active fluids (8), much less is known about how we can control or harness such collective phenomena to achieve functional goals. Recent experimental advances in microfabrication and optogenetic techniques have allowed the development of novel bacterial and synthetic reconstituted systems to begin addressing this question in different contexts, such as active engines for efficient work extraction (9, 10), the dynamic control of reconfigurable density patterns (11, 12), and the targeted creation and transport of localized structures such as defects (13, 14). On a different scale, the collective control of migrating and proliferating cellular monolayers through patterned substrates (15, 16) or external fields (17, 18) also presents new possibilities for the control of active biological matter.

The capacity for spontaneous and autonomous motion in active fluids raises a natural question: What are the optimal strategies to spatially transport active materials? The general problem of optimal mass transport—i.e., finding the easiest or cheapest way to move mass from one place to another—has been explored for over two centuries (19, 20) with deep connections to economics, hydrodynamics, machine learning, etc. (20–22). But much less is known about how to optimally transport physical materials, such as active fluids, that obey complex spatiotemporal dynamics, leading us to ask: How can we construct and understand optimal transport policies to move active matter?

Here, we pose this question in the simplest setting of transporting an active drop by dynamically controlling its internal activity in space–time. By incorporating the dynamical constraints of droplet motion using the lubrication approximation and expressing the cost of transport in terms of the dissipation rate, we ask if we can determine the internal activity to move the drop from one place to another while minimizing the total dissipation, thus bringing it within the framework of optimal control theory.

By projecting the continuum description of droplet motion onto a finite-dimensional slow manifold, we derive a reduced system of ordinary differential equations (ODEs) for the position and size of the droplet. Interestingly, for a range of parameters, an intuitive “gather–move–spread” style strategy emerges naturally as an optimum within our framework. Numerical simulations of the continuum equations using an evolutionary algorithm to determine the optimal activity profile confirm the qualitative nature of the results obtained from the reduced order model. Together, these solutions provide a comprehensive, yet interpretable, framework (Fig. 1) to understand the optimal solutions obtained and highlights the resulting trade-offs between cost, transport precision, and efficiency that can be tuned by the interplay of passive and active stresses in the system.

## Significance

Transportation, in its broadest sense, is an important task in many fields, including engineering, physics, biology, and economics, and a great deal is known about optimal and efficient strategies to move matter, energy, and information around. But can we craft similar optimal protocols to transport autonomously moving (active) matter, such as self-propelled drops or migrating cells? We develop an optimal control framework to transport active fluid drops with the least amount of energy dissipated, by manipulating the spatio-temporal profile of its internal active stresses. By combining numerical solutions and analytical insight, we uncover simple principles and characteristic trade-offs that govern the optimal policies, suggesting general strategies for optimal transportation in a wide variety of synthetic and biological active systems.

Author affiliations: <sup>a</sup>Department of Physics, Harvard University, Cambridge, MA 02138; <sup>b</sup>Paulson School of Engineering and Applied Sciences, Harvard University, Cambridge, MA 02138; and <sup>c</sup>Department of Organismic and Evolutionary Biology, Harvard University, Cambridge, MA 02138

Author contributions: L.M. conceived of research; V.R., S.S., and L.M. formulated and solved the ODE optimal control problem; S.S. and L.M. formulated and solved the PDE control problem; S.S., V.R., and L.M. analyzed data; and S.S., V.R., and L.M. wrote the paper.

The authors declare no competing interest.

This article is a PNAS Direct Submission.

Copyright © 2022 the Author(s). Published by PNAS. This article is distributed under [Creative Commons Attribution-NonCommercial-NoDerivatives License 4.0 \(CC BY-NC-ND\)](https://creativecommons.org/licenses/by-nc-nd/4.0/).

<sup>1</sup>S.S. and V.R. contributed equally to this work.

<sup>2</sup>To whom correspondence may be addressed. Email: [lmahadev@g.harvard.edu](mailto:lmahadev@g.harvard.edu).

This article contains supporting information online at <https://www.pnas.org/lookup/suppl/doi:10.1073/pnas.2121985119/-DCSupplemental>.

Published August 24, 2022.

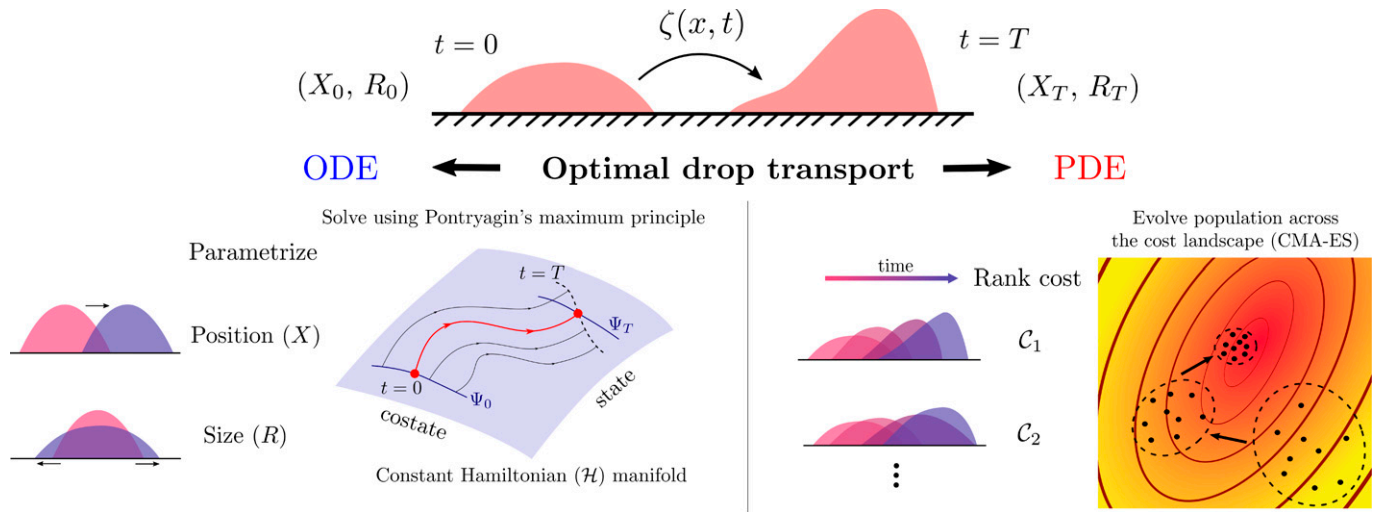


**Fig. 1.** Optimal transport of an active drop. A schematic illustrating our framework to solve the problem of transporting an active drop by minimizing a specified cost function, such as the mechanical work. The spatiotemporal profile of activity  $\zeta(x, t)$  is the control variable, and the transport task involves moving the drop from position  $X_0$  and size  $R_0$  to a final position  $X_T$  and size  $R_T$  in a finite time  $T$ . We employ two complementary approaches: 1) finite-dimensional optimal control using Pontryagin's maximum principle on an ODE-based reduced order model that captures parametrized features of the drop; and 2) constrained numerical optimization of the nonlinear continuum PDE using a gradient-free evolutionary algorithm, such as CMA-ES (see *PDE Control* main text).

## Mathematical Model for Optimal Droplet Transport

**Lubrication Dynamics of an Active Drop.** We describe the dynamics of a slender drop of an active suspension on a solid surface in the asymptotic limit exemplified by viscous lubrication theory (23, 24, 25). For simplicity, we consider a two-dimensional (2D) drop moving in the  $x$  direction (see Fig. 2) and neglect gravity by assuming the drop size to be smaller than the capillary length. Fluid incompressibility requires that  $\nabla \cdot \mathbf{u} = \partial_x u + \partial_z v = 0$ , where  $\mathbf{u} = (u(x, z, t), v(x, z, t))$  is the local flow velocity. Upon depth integrating the incompressibility equation, and noting the free surface boundary condition  $v|_{z=h} = \partial_t h + u \partial_x h|_{z=h}$ , where  $h(x, t)$  is the height profile of the drop, we obtain the conservation law

$$\partial_t h + \partial_x q = 0. \quad [1]$$

Here, the mass flux  $q = h \langle u \rangle$ , with the average horizontal velocity  $\langle u \rangle = (1/h) \int_0^h dz u$ . Assuming that there is no addition

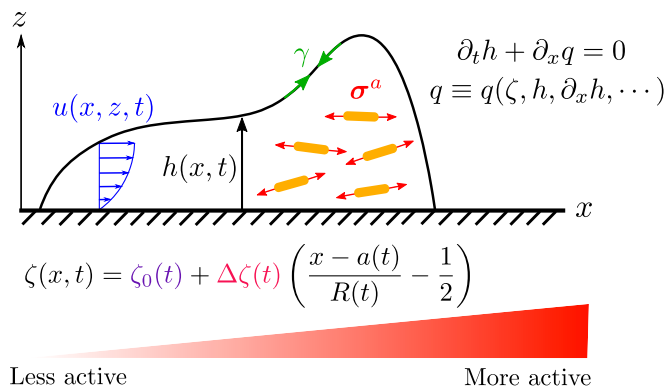


**Fig. 2.** Model of an active drop moving on a substrate. The horizontal flow velocity  $u(x, z, t)$  driven by active internal stresses ( $\sigma^a$ ) and surface tension ( $\gamma$ ) adopts a Poiseuille-like profile in the drop interior, characteristic of lubrication theory. The drop height  $h(x, t)$  obeys the continuity equation (Eq. 1) with a flux  $q$  that encodes the constitutive relation (Eq. 3) for how activity drives fluid flow. The spatial profile of activity ( $\zeta(x, t)$ ) is a simple linear ramp with a constant offset, allowing for both drop translation and size change (Eq. 7).

or loss of mass of the drop, we can write this as a global condition

$$\int dx h(x, t) = 1, \quad [2]$$

to fix our units of length.

In the low-Reynolds-number regime appropriate for small viscous drops, we operate in the Stokesian limit, wherein force balance implies  $\nabla \cdot \boldsymbol{\sigma} = \mathbf{0}$ , where the total stress  $\boldsymbol{\sigma} = -p\mathbf{I} + \eta[\nabla \mathbf{u} + (\nabla \mathbf{u})^T] + \boldsymbol{\sigma}^a$  is the sum of the pressure  $p$ , a viscous stress (in a liquid with shear viscosity  $\eta$ ), and an active stress. We assume that the active stress  $\boldsymbol{\sigma}^a = \zeta h (\hat{\mathbf{n}}\hat{\mathbf{n}} - \mathbf{I}/2)$  (8, 26) is proportional to the local density  $\sim h$ , while depending on the local orientation  $\hat{\mathbf{n}}$  of anisotropic active agents.\* The activity  $\zeta(x, t)$  depends on space and time and originates from the density of force dipoles exerted by elongated active units, which can be of either sign, with  $\zeta > 0$  for contractile systems and  $\zeta < 0$  for extensile systems. This form of the active stress is applicable to drops of coherently swimming dense bacterial suspensions or ordered collections of motor-protein-driven cytoskeletal filaments present in synthetic drops or living cells (23, 24). For simplicity, we shall assume strong ordering along the horizontal direction and neglect any rapid orientational relaxation to set  $\hat{\mathbf{n}} \simeq \hat{\mathbf{x}}$  to lowest order in gradients ( $|\partial_x h| \ll 1$ ). The active forcing nonetheless survives in this limit, as the active stress directly depends on the local density of the drop ( $\sim h$ ), unlike previous models (23, 24) that rely on splay-bend deformations of orientational order.

In the lubrication limit corresponding to a slender drop,  $|\partial_x h|^2 \ll 1$ , so that we can neglect longitudinal flow gradients as  $|\partial_x^2 u| \ll |\partial_z^2 u|$  and  $|\partial_x v| \ll |\partial_z v|$ . Then, the stress in the fluid is dominated by the pressure, which is determined by the capillary boundary condition on the drop surface  $\sigma_{zz}|_{z=h} = \gamma \partial_x^2 h$ , where  $\gamma$  is the interfacial tension and yields  $p = -(\zeta/2)h - \gamma \partial_x^2 h$ . Using this in the horizontal force-balance equation, along with the no-slip ( $u|_{z=0} = 0$ ) and free surface ( $\partial_z u|_{z=h} = 0$ ) boundary conditions, yields the horizontal velocity profile  $u = z((2h - z))\partial_x \sigma / 2\eta$ , where  $\sigma = \zeta h + \gamma \partial_x^2 h$  is the effective

\*An isotropic active pressure that is constant across the thickness of the drop does not change anything, as it can be absorbed into  $p$ .

uniaxial stress. Averaging the velocity through the thickness of the drop shows that the net flux is

$$q = h\langle u \rangle = \frac{h^3}{3\eta} \partial_x (\zeta h + \gamma \partial_x^2 h). \quad [3]$$

Eqs. 1 and 3 complemented by boundary and initial conditions on the height of the film and its derivatives completely describe the macroscopic dynamics of an active drop on a substrate, once the activity field  $\zeta(x, t)$  is specified. For finite drops, in the neighborhood of the contact line, the boundary conditions associated with partial slip, prewetting films, and/or finite contact angles have to be accounted for (27, 28) (*SI Appendix*). In our formulation, the passive surface tension  $\gamma$  serves to regulate the drop curvature, while the (controllable) activity  $\zeta(x, t)$  enters as an unknown spatiotemporally varying nonlinear diffusivity, but is analogous to gravity (27).

**Optimal Transport.** The optimal transport of an active drop requires finding an actuation protocol for the activity profile  $\zeta(x, t)$  that moves the drop at a minimal cost. We choose a physically motivated cost  $\mathcal{C} = \mathcal{W} + \mathcal{T}$ , which includes two terms, an integrated bulk cost that tracks the total mechanical work ( $\mathcal{W}$ ) done by the active and passive forces and a terminal cost ( $\mathcal{T}$ ) that penalizes any discrepancy between the final and desired state of the drop. Within the lubrication approximation, the viscous dissipation in the drop  $\sim \eta(\partial_z u)^2$  is dominated by shear, so that the total mechanical work is given by

$$\mathcal{W} = \int_0^T dt \int dx \frac{h^3}{3\eta} (\partial_x \sigma)^2. \quad [4]$$

As expected, the total amount of energy expended and lost via dissipation by the system is always nonnegative ( $\mathcal{W} \geq 0$ ). We note that this is equivalent to stating that the effective mechanical energy in the drop  $E = (1/2) \int dx [\gamma(\partial_x h)^2 - \zeta h^2]$  satisfies the condition  $dE/dt = - \int dx (h^3/3\eta)(\partial_x \sigma)^2 < 0$  if  $\partial_t \zeta = 0$  and boundary fluxes are absent—i.e., the system is dissipative. The work done by the active stress alone ( $\mathcal{W}_a = \int_0^T dt \int dx h\langle u \rangle \partial_x (\zeta h)$ ), on the other hand, is not guaranteed to be a well-behaved cost function, as  $\mathcal{W}_a$  can be of either sign in general (though  $\mathcal{W}_a = \mathcal{W} \geq 0$  when  $\gamma = 0$ ), reflecting the possibility of both energy consumption and extraction from the nonequilibrium system (29). Here, we have not included the energy cost required to maintain the active machinery (30); in the simplest setting, this is proportional to the total amount of the active fluid, which, in our case, is a constant.

For simplicity, we have assumed that the total time duration  $T$  is fixed, though other strategies, such as minimal time control, are possible. However, we do account for a terminal cost to minimally capture the intent of the task, which is to translate the drop by a fixed distance and control its final spread as well. We incorporate this in a simple quadratic term

$$\mathcal{T} = \mu_X \left( \frac{X(T) - X_T}{X_T} \right)^2 + \mu_R \left( \frac{R(T) - R_T}{R_T} \right)^2, \quad [5]$$

where  $X_T$  and  $R_T$  are the desired values for the drop center of mass and the drop size at the end of the transport. The corresponding penalties are  $\mu_X$  and  $\mu_R$  for the terminal position and size terms. As mentioned previously, the drop has compact support and finite size, which is denoted by  $R(t)$ , and its position is given by the center of mass, namely,

$$X(t) = \int dx x h(x, t), \quad [6]$$

both of which can be evaluated at the final time  $t = T$  to compute  $\mathcal{T}$  (Eq. 5). We will always set the initial position of the drop to be at the origin,  $X(0) = 0$ , without loss of generality.

It is worthwhile to pause here to compare our formulation of optimal droplet transport with the classical Monge–Kantorovich formulation of optimal transport (19–22). Unlike the conventional formulation, where the sole constraint is global mass conservation (Eq. 2), here, we constrain the dynamics to account for both local mass and momentum conservation. The latter is a direct consequence of the physics of fluid motion that dictates how the material responds to local actuation of active stresses, as specified by Eqs. 1 and 3. As a result, our transport plan does not simply rely on a registration solution of a static Monge–Ampère equation (20). A further salient feature worth emphasizing is the parabolic (diffusive) nature of our dynamics, where the control (activity) enters as a nonlinear diffusivity by virtue of the geometric reduction intrinsic to drops and thin films. This is distinct from the hyperbolic (advective) setting present in Benamou–Brenner-style formulations (22) that employ a hydrodynamic analogy between optimal transport and inviscid fluid flow, where the velocity field is the control variable.

## Protocol for Optimal Droplet Transport

With this minimal physical framework in hand, how can we compute the optimal transport policies? We choose two different routes of solving the problem (Fig. 1). First, we project our nonlinear partial differential equation (PDE) for the drop dynamics (Eqs. 1 and 3) onto a finite number of low order modes that correlate with the location, size, and shape of the droplet. We propose a strategy that minimizes or eliminates drift terms in the reduced description by considering the active controlled dynamics within a low-dimensional slow manifold that is approximately invariant to the passive (noncontrolled) forces. The resulting ODEs can then be handled using standard optimal control theory (31), which we solve both analytically and numerically. We then compare this reduced order description to the full PDE model, for which we analyze the optimal control problem numerically. However, unlike conventional forward problems that are solved with initial values in time, the controlled dynamics requires the solution to a much harder boundary-value problem in time. One way to solve this problem is to stochastically search for different initializations using a large number of forward runs to find an appropriate solution satisfying the required boundary condition. We implement this using a gradient-free covariance matrix adaptation evolution strategy (CMA-ES) (32), as explained later and in *SI Appendix*.

**ODE Control.** For simplicity, we consider a minimal setting, where the spatial variation of the activity is fixed, but its time variation is arbitrary. As we are primarily interested in controlling the position and size of the drop, the simplest spatial variation of activity that can accomplish both is a linear profile,

$$\zeta(x, t) = \zeta_0(t) + \Delta\zeta(t) \left( \frac{x - a(t)}{R(t)} - \frac{1}{2} \right), \quad [7]$$

where  $\zeta_0(t)$  is a time-varying mean activity and  $\Delta\zeta(t)$  is a time-varying gradient in activity (Fig. 2). We choose this specific form, which depends explicitly on the drop size  $R(t)$  and the position of the left edge of the drop  $a(t)$ , so that the (spatial) average activity in the drop is  $(1/R(t)) \int_{h>0} dx \zeta(x, t) = \zeta_0(t)$ . We note that while  $\zeta_0$  essentially controls the size of the drop, with  $\zeta_0 > 0$

leading to contraction and  $\zeta_0 < 0$  leading to expansion, the linear gradient in activity  $\Delta\zeta$  controls the drop translation, the direction of which is determined by the sign of  $\Delta\zeta$ . In contrast with recent works that have explored bulk contractility driven crawling of cells (25, 33) and shown how it optimizes the mechanical efficiency of steady motion (30), here, we address the unsteady dynamics and its control problem.

The relative importance of the active drive versus surface tension is quantified by a dimensionless active capillary number

$$\text{Ca}_\zeta = \left\langle \frac{|\Delta\zeta(t)|R(t)^2}{\gamma} \right\rangle_T, \quad [8]$$

where the time average  $\langle A \rangle_T = (1/T) \int_0^T dt A$ . As will be clear later, Eq. 8 is akin to the conventional definition of a capillary number (28), only now with the velocity scale set by the activity gradient ( $\Delta\zeta$ ), which is essential to drive drop motion.<sup>†</sup> For large  $\text{Ca}_\zeta \gg 1$ , active forcing dominates surface tension, and we can safely neglect boundary effects, while for  $\text{Ca}_\zeta \sim 1 - \mathcal{O}(10)$ , active and passive forces compete, and the equations have to be generalized to include the dynamics of the contact lines, as detailed in *SI Appendix*.

We project the nonlinear PDE (Eqs. 1 and 3) onto a truncated set of modes that we choose so that the resulting ODE system is as drift-free as possible—i.e., the system lacks dynamics in the absence of the controls (here, activity). This is achieved by noting that the flux due to capillary forces vanishes when  $\partial_x^3 h(x, t) = 0$ , and the drop adopts a parabolic profile. This permits a simple parametrization of the drop profile via two modes of deformation—a translation in the center of mass  $X(t)$  and a change in the size  $R(t)$ , which, along with Eq. 2, gives

$$h(x, t) = \frac{6}{R(t)^3} \left[ \frac{R(t)^2}{4} - (x - X(t))^2 \right]. \quad [9]$$

Note that  $h(x, t) = 0$  at the two ends of the drop,  $x = X(t) \pm R(t)/2$ , and vanishes outside this region. While translation is a genuine zero mode of capillarity, size change of the drop is only an approximate zero mode that is violated near the boundaries where wetting and contact-angle physics become important (28). Nonetheless, by focusing on the bulk dynamics, we obtain a 2D manifold spanned by  $X(t)$  and  $R(t)$  that remains approximately invariant under the action of capillary forces.

Employing a Galerkin approximation (i.e., projecting onto a local polynomial basis) allows us to compute spatial moments of the flux  $q(x, t)$  and project the continuum equations onto this manifold to obtain a pair of nonlinearly coupled ODEs (*SI Appendix*)

$$\dot{X}(t) = \frac{18\Delta\zeta(t)}{35\eta R(t)^4}, \quad \dot{R}(t) = -\frac{24\zeta_0(t)}{7\eta R(t)^4}. \quad [10]$$

As expected, the mean ( $\zeta_0$ ) and gradient ( $\Delta\zeta$ ) components of the active stress independently control the drop size and position, respectively. By construction, surface tension  $\gamma$  is absent in Eq. 10, and the equation is drift-free. The existence of optimal controls is predicated on an important property of the dynamics, namely, controllability (34, 35)—i.e., the existence of a path connecting any two points in the state or configuration space, spanned here

<sup>†</sup> Similarly, we can define an active Bond number  $\text{Bo}_\zeta = \langle |\zeta_0(t)|R(t)^2/\gamma \rangle_T$  to characterize the relative importance of the average activity (associated with size change) compared to surface tension. Since  $\text{Ca}_\zeta$  is more directly relevant for transport and in most of our results—for instance, in Fig. 4, both  $\text{Bo}_\zeta$  and  $\text{Ca}_\zeta$  are empirically correlated (not shown), we do not consider the active Bond number any further.

by  $X$  and  $R$  (see *SI Appendix* for a more detailed explanation). As the two controls ( $\zeta_0, \Delta\zeta$ ) enter linearly and independently, and the dynamics has no fixed points for nonvanishing controls, one can easily confirm that Eq. 10 is controllable, allowing us to guarantee the ability to steer the system from any state to any other state within the space of drop configurations labeled by  $(X, R)$ . The absence of any drift (control-independent) terms presents a technical advantage, as the system permits a global, rather than local, notion of controllability, even when the dynamics is nonlinear (*SI Appendix*), thereby justifying our mode-reduction strategy.

For simplicity, we consider the fixed end point problem where the terminal conditions are imposed strictly ( $X(T) = X_T, R(T) = R_T$ ), in which case the total cost reduces to the net dissipation ( $\mathcal{C} = \mathcal{W}$ ). The drop parametrization (Eq. 9) allows us to easily compute the dissipation rate to be

$$\mathcal{L} = \frac{1}{\eta R^6} \left[ \frac{72}{35} \zeta_0^2 + \frac{54}{77} \Delta\zeta^2 \right], \quad [11]$$

whose time integral gives the cost ( $\mathcal{W} = \int_0^T dt \mathcal{L}$ ). As expected, we obtain a simple sum of squares in terms of the two active drives, along with a strong size dependence arising from the geometry of the drop. To solve the optimal control problem, we employ Pontryagin's Maximum Principle that provides the necessary conditions for optimality (36) (see *SI Appendix* for a brief summary). Upon introducing the costates (Lagrange multipliers)  $p_X(t)$  and  $p_R(t)$  to enforce the dynamical constraints in Eq. 10, a necessary condition for optimality is the maximization of the control Hamiltonian

$$\mathcal{H} = p_X \frac{18\Delta\zeta}{35\eta R^4} - p_R \frac{24\zeta_0}{7\eta R^4} - \mathcal{L}, \quad [12]$$

with respect to the controls (*SI Appendix*). This gives  $\zeta_0^* = -5p_R R^2/6$  and  $\Delta\zeta^* = 11p_X R^2/30$ , which, when substituted back into Eq. 12, gives the conserved Hamiltonian  $H = \mathcal{H}(\zeta_0^*, \Delta\zeta^*)$ . The candidate extremals for the optimal control problem satisfy Hamiltonian dynamics in terms of the state variables ( $\dot{X} = \partial_{p_X} H, \dot{R} = \partial_{p_R} H$ ) and corresponding costates ( $\dot{p}_X = -\partial_X H, \dot{p}_R = -\partial_R H$ ). For the state variables, this gives back Eq. 10 driven now by the optimal controls ( $\zeta_0^*, \Delta\zeta^*$ ); translational invariance enforces that  $\partial_X \mathcal{H} = 0$ ; hence,  $p_X$  is conserved along the optimal trajectory.

These coupled dynamical equations along with the initial and terminal conditions can be solved analytically to obtain the optimal transport protocols (*SI Appendix*) to displace an active drop by a distance  $X_T$  and change its size from  $R_0$  to  $R_T$  in a finite time interval  $T$ . A representative solution is plotted in Fig. 3A and B for  $X_T = 0.8, R_0 = \sqrt{6}$  and  $R_T = 3$ . The first-order necessary conditions generally allow for nonuniqueness of the candidate extrema, but we only show the global optimizer in Fig. 3. For the chosen parameters, the optimal protocol leads to a nonmonotonic change in drop size (Fig. 3B), first decreasing and later increasing to reach the final size  $R_T$ . This is reflected in the sign change of the mean active stress  $\zeta_0$  (Fig. 3A), which switches from being contractile initially ( $\zeta_0 > 0$ ) to extensile at later times ( $\zeta_0 < 0$ ). The drop translates smoothly with a maximal velocity precisely when the drop size is the smallest, even though the drive ( $\Delta\zeta$ ) is minimal at this point (Fig. 3A). Hence, the drop executes a continuous version of an intuitive gather–move–spread-like strategy that naturally emerges as an optimal transport plan in our framework. A simple concentration effect that enhances the active drive in smaller drops underlies this phenomenon by allowing for faster

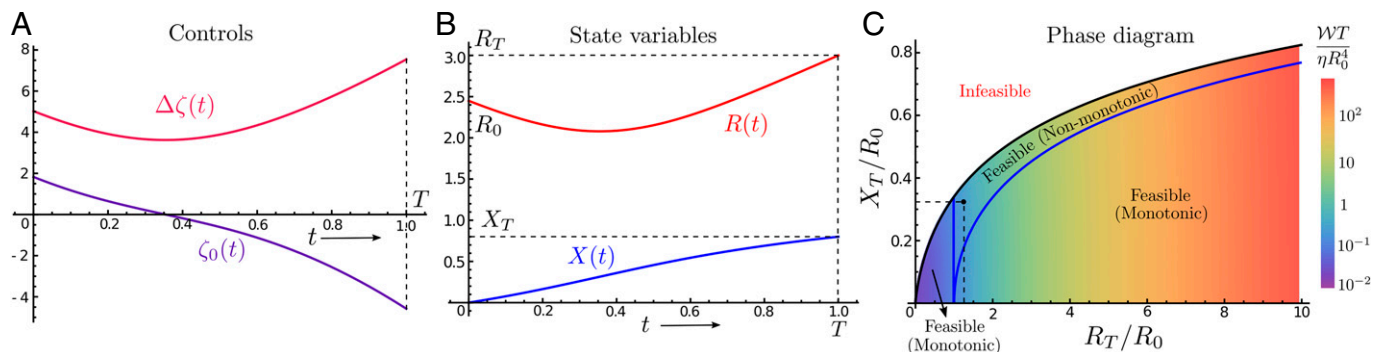


**Fig. 3.** ODE optimal control. (A and B) Sample trajectories for the globally optimal mean ( $\zeta_0$ ) and gradient ( $\Delta\zeta$ ) activity are shown in A, and the associated controlled dynamics for the drop position ( $X$ ) and size ( $R$ ) are shown in B. The parameters chosen are  $X_T = 0.8$ ,  $R_0 = \sqrt{6}$ ,  $R_T = 3$ ,  $T = 1$ , and  $\eta = 0.1$ . Note that as  $\eta$  sets a time scale, only the ratio  $T/\eta$  is important. For these parameter values, we see that the size change is nonmonotonic, which is reflected in the sign change in the mean activity  $\zeta_0(t)$ . The initial contractile activity ( $\zeta_0 > 0$ ) causes the drop to shrink and consequently accelerate its translation, and, later, the activity switches over to become extensile ( $\zeta_0 < 0$ ) to allow the drop to reach its larger final size  $R_T$ . (C) The phase diagram here represents the feasibility region for optimal transport of a parabolic active drop, as a function of the nondimensionalized drop displacement ( $X_T/R_0$ ) and its size disparity ( $R_T/R_0$ ). The black curve is the maximum achievable displacement  $X_T$  for a given relative change in size ( $R_T/R_0$ ), beyond which no smooth optimal controls exist. Below the black curve is the feasible region, with the shaded color representing the total work done [nondimensionalized as  $\mathcal{WT}/(\eta R_0^4)$ ] by the globally optimal policy, with the cost increasing from blue to red. The blue curves in the shaded region demarcate the parameter space where the global optimizer has a monotonic or nonmonotonic size dependence as a function of time. Nonmonotonic changes in size are favored in the region bordered by the blue and black curves and only occur when  $R_T > R_0$ . For  $R_T < R_0$ , the optimal policies have a monotonic size dependence. The black dot corresponds to the solution shown in A and B.

transport at lower activity. Our solution reveals a further striking result—for certain values of the target parameters (set by  $X_T$  and  $R_T$ ) with strict terminal constraints, no continuous optimal policies for the transport problem exist! This does not contradict the fact that the dynamical system (Eq. 10) is controllable, but, rather, highlights a subtlety. While controllability guarantees the presence of a trajectory in configuration space that steers the drop to its desired final state, and hence the existence of optimal controls, it does not, in general, guarantee that this transport is either continuous or achievable in finite time.

As shown by the colored region bounded by the black curve in Fig. 3C, we have a feasible or reachable regime, where smooth optimal solutions exist and the net dissipation is finite (shown in the heat map, with the cost increasing from blue to red), while in the infeasible region, no smooth solution satisfies the terminal conditions. The blue curve in Fig. 3C further demarcates the parameter regime where the global optimum corresponds to policies with a monotonic change in drop size, where the mean activity ( $\zeta_0$ ) maintains a fixed sign. These appear either for sufficiently small displacements or when the final drop size is smaller than the initial one ( $R_T < R_0$ ). Nonsmooth protocols can be constructed to access points in the infeasible region in Fig. 3C, but they lack a natural parametrization. As a result, the search for an optimal policy in this larger function space is analytically intractable, and we focus only on smooth protocols for simplicity. The feasibility curve can alternatively be viewed as solving a maximin problem, where we maximize the minimum dissipation protocol over the translation  $X_T$  for a fixed change in drop size ( $R_T/R_0$ ), the solution for which roughly equipartitions the transport cost (black curve in Fig. 3C; see SI Appendix for further details).

Keeping surface tension  $\gamma = 0$ , we can extend this analysis to include simple variations in drop shape via a spatial asymmetry of the height profile and numerically solve the optimal control problem using CasADi (37) and numerical continuation schemes (see SI Appendix for details). Our results show that while small variations in the drop asymmetry result in smooth optimal policies, similar to those in Fig. 3A, larger values of drop asymmetry lead to short-wavelength numerical instabilities, as expected when the surface tension vanishes. Thus, while the dynamics of drop position and size are captured by the simple ODE model (Eq. 10), the dynamics of drop shape requires us to account for the inclusion

of capillary effects for stability. To accomplish this, we switch to solving the full PDE model.

**PDE Control.** As the PDE model permits complex shape change of the drop, we lift the restriction of the controlled dynamics on the slow manifold selected by capillarity and allow arbitrary shape variations by tuning  $\gamma$  (conversely,  $\text{Ca}_\zeta$ ; Eq. 8). In order to select smooth control policies, we generalize the cost function  $\mathcal{C} = \mathcal{W} + \mathcal{T} + \mathcal{R}$  (SI Appendix) to include a regularizing term  $\mathcal{R}$  in addition to the total dissipation ( $\mathcal{W}$ ; Eq. 4) and a finite terminal cost ( $\mathcal{T}$  with  $\mu_X, \mu_R < \infty$ ; Eq. 5). The regularizing cost  $\sim \int dt \int dx (\partial_t \zeta)^2$  penalizes large temporal variations in activity (SI Appendix), and it implements a version of minimal attention control (38). In the presence of a finite surface tension  $\gamma$ , we must also correctly implement contact-line motion at the boundary of the drop, which we do by simply introducing a thin precursor film that coats the entire surface and a disjoining potential (27) that sets both the film thickness and the equilibrium contact angle of a sessile drop (see SI Appendix for details). These additional terms are negligible in the bulk of the drop, but are dominant near the contact lines, which will become important when active and capillary forces are comparable ( $\text{Ca}_\zeta \lesssim \mathcal{O}(10)$ ), similar to recently explored scenarios the context of steady migration of cells (25) in the absence of any dynamic control.

We numerically integrate the dynamical equations using a finite element method implemented using the FEniCS open-source package (39, 40) and perform constrained optimization using a gradient-free CMA-ES (32) (see SI Appendix for details). Multiple runs are sequentially minimized with independent initializations for the activity profile, and we choose the lowest-cost solution as an estimate for the optimum. As before, the drop is initially at the origin ( $X_0 = 0$ ) with a size  $R_0 = \sqrt{6}$ , which corresponds to an equilibrium contact angle of  $\phi_{\text{eq}} = \pi/4$ . The viscosity  $\eta = 0.1$  and total time  $T = 1$  are fixed in all the runs. To probe the caliber of the optimal policies obtained across tasks of increasing difficulty, we vary the imposed drop translation  $X_T$  along with the surface tension  $\gamma$ .

For small surface tension or strong active driving (large  $\text{Ca}_\zeta$ ), the dynamics of the drop is dominated by bulk dissipation. A typical trajectory of the drop profile (Movie S1) and the controls is shown in Fig. 4A, for  $X_T = 0.8$  and  $\text{Ca}_\zeta \sim 383$ . The drop

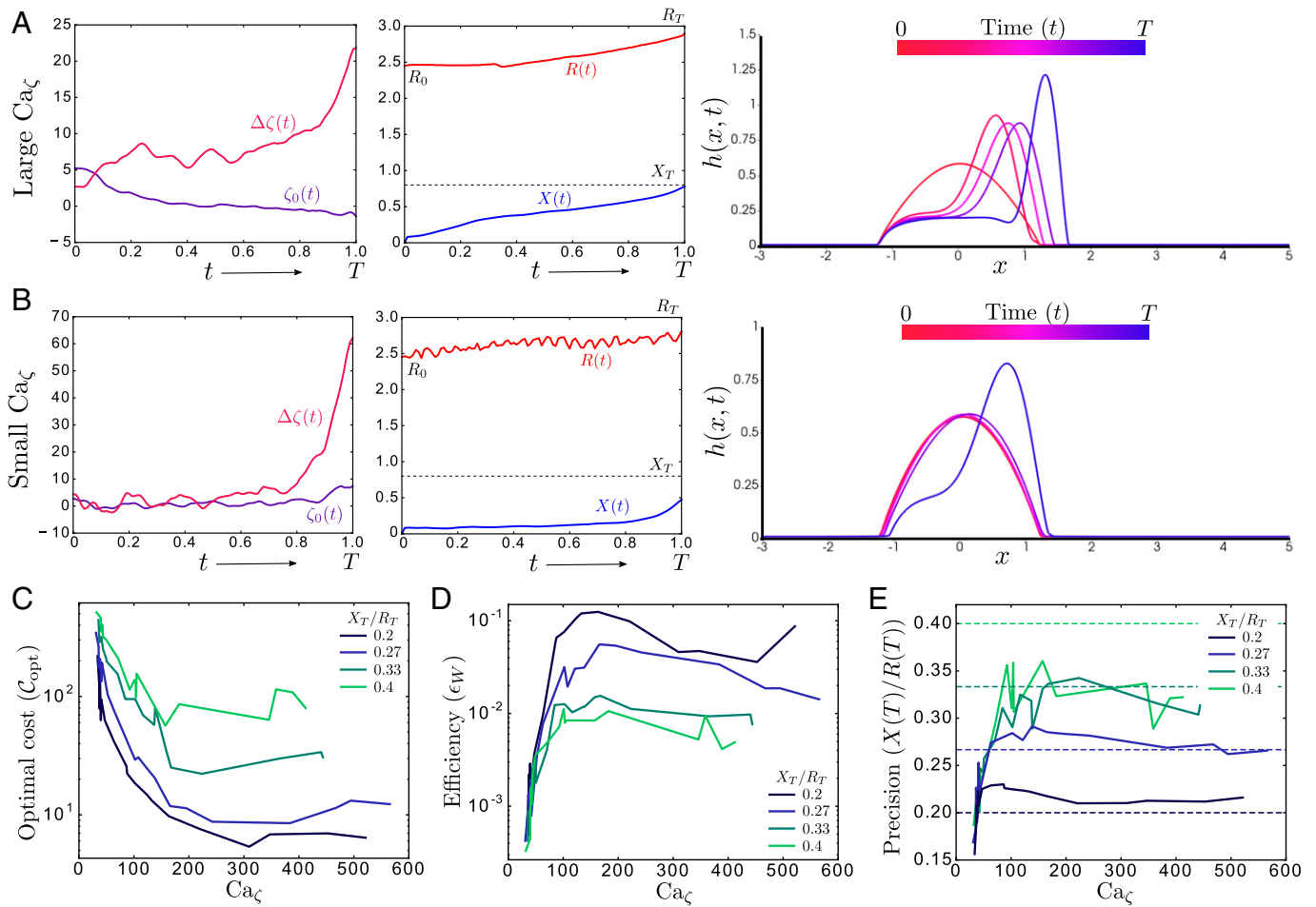


**Fig. 4.** PDE optimal control. (A) The optimal activity controls ( $\zeta_0(t)$ ,  $\Delta\zeta(t)$ ; *Left*) and corresponding trajectories for the state variables ( $X(t)$ ,  $R(t)$ ; *Center*) and the full drop profile ( $h(x, t)$ ; *Right*), obtained by numerical optimization for small surface tension or large active capillary number ( $\gamma = 0.15$ ,  $Ca_c = 383.66$ ). The drop adopts a strongly asymmetric shape, with an advancing peak and receding tail, like in ref. 25. (B) Similar plots with the optimal activity controls ( $\zeta_0(t)$ ,  $\Delta\zeta(t)$ ; *Left*), and corresponding drop trajectory ( $X(t)$ ,  $R(t)$ , *Center*;  $h(x, t)$ , *Right*), now obtained for large surface tension or small active capillary number ( $\gamma = 2$ ,  $Ca_c = 30.91$ ). The transport plan fares poorly as the drops fails to reach the desired final position and size and wastes a significant amount of energy in futile size oscillations ( $R(t)$ ; *Center*) that don't aid in transport. Both A and B are computed by using  $X_T = 0.8$  and  $R_T = 3$  ( $X_0 = 0$  and  $R_0 = \sqrt{6}$  is kept fixed throughout), though similar policies are obtained for other values of  $X_T/R_T$  as well. (C–E) The total cost ( $C_{opt}$ ; C), efficiency ( $\epsilon_W$  [Eqs. 13 and 14]; D), and precision ( $X(T)/R(T)$ ; E) of the numerically computed optimal transport protocol plotted against  $Ca_c$ , for different tasks labeled by increasing  $X_T/R_T$  (blue to green). Remarkably, the performance curves present an optimal trade-off in balancing active forces against passive ones to attain improved drop transport plans at intermediate values of  $Ca_c$ .

develops a prominent advancing peak and a thin receding tail (Fig. 4 A, *Right* and [Movie S1](#)), similar to steadily translating drop shapes recently obtained in ref. 25. The optimal controls and the drop motion vary smoothly (Fig. 4 A, *Left* and *Center*) and successfully accomplish the transport task. Although the drop undergoes dramatic shape changes, the optimal controls are qualitatively consistent with our ODE results (Fig. 3 A and B). In particular, we note that the mean activity ( $\zeta_0$ ) changes sign, switching from contractile to extensile activity, as predicted by our reduced order description (Fig. 3A). For further comparison, we also simulate the continuum drop dynamics ([Movie S2](#)), using the optimal activity profile supplied by the ODE solution (Fig. 3A) for the same parameters. In the regime of applicability of the reduced order model (corresponding to low values of the surface tension or, equivalently, large  $Ca_c$ ), the resulting drop trajectory ([Movie S2](#)) is qualitatively consistent with the solution obtained from the PDE optimization (Fig. 4A and [Movie S1](#)); larger values of surface tension (smaller  $Ca_c$ ) lead to a qualitatively different scenario. As shown in Fig. 4B and [Movie S3](#), for  $X_T = 0.8$  and  $Ca_c \sim 31$ , the drop remains nearly stationary for a finite time period, after which it advances by a small amount. This is reminiscent of “waiting-time” solutions (41) that are present

in nonlinear diffusion equations of the form we have here. The drop performs rapid small-scale oscillations of its shape and size (Fig. 4 B, *Center* and *Right* and [Movie S3](#)) that arise from a competition between the active and passive (capillary) forces. While the active controls drive droplet motion, surface tension and substrate wetting resist variations in the drop shape and the contact angle, thereby limiting the translation achieved by the drop. The resulting “futile” oscillations wastefully dissipate large amounts of energy, performing poorly in the transport task (Fig. 4 B, *Left* and *Center*). We note that in all the examples studied, only the final drop position ( $X(T)$ ) and size ( $R(T)$ ) are constrained, but the final shape is not. Nonetheless, upon cessation of the activity protocol, surface tension will cause the drop to round up into a parabolic shape (just as it started out) without any additional energy injection. This allows for a simple way to recover the sessile drop shape at the end. Although this passive relaxation will inevitably incur drop translation due to its asymmetric shape, by extending the control protocol (and, hence, expending additional energy), it should be possible to compensate for this passive drop recoil.

The varied optimal strategies obtained upon tuning surface tension suggests a potential trade-off between active and passive

forces. While large  $Ca_\zeta$  allows for robust and efficient transport, it also generates dramatic shape changes, which dissipate excessive energy. Smaller  $Ca_\zeta$  restricts shape change, but consequently dissipates energy into futile oscillations that fail to complete the transport task. This suggests that an intermediate surface tension or  $Ca_\zeta$  would serve as the best choice to tune the optimal transport plan by balancing active and passive forces. To quantify this trade-off, we employ three different performance metrics as a function of  $Ca_\zeta$  and the task difficulty characterized by increasing  $X_T/R_T$ . The first is simply the total cost of the optimal solution ( $\mathcal{C}_{\text{opt}}$ ), plotted in Fig. 4C. Second, we use a simple measure of efficiency ( $\epsilon_W$ ) to quantify the excess dissipation in the optimal solution (Fig. 4D). We note that, for any arbitrary drop trajectory starting at the origin, there is a minimal amount of work that must necessarily be expended, given by (see *SI Appendix* for a derivation)

$$\mathcal{W}_{\min} = \frac{3\eta}{2T\|h\|_\infty^2} \left[ X(T)^2 + \frac{(\Delta(T) - \Delta(0))^2}{4\langle\Delta\rangle_T} \right], \quad [13]$$

where  $\|h\|_\infty = \sup_{x,t} h(x,t)$  is the maximum value of the drop height attained throughout its trajectory and  $\Delta(t) = \int dx (x - X(t))^2 h(x,t)$  is the variance in the drop height, which is related to the size of the drop ( $\Delta \propto R^2$ ). Note that Eq. 13 is independent of the rheology and constitutive law for the fluid stress and simply relies on the existence of a flux  $q(x,t)$  that directly determines the dissipation (*SI Appendix*). As the work done in the optimal solution is bounded below by construction ( $\mathcal{W}_{\text{opt}} \geq \mathcal{W}_{\min}$ ), we define the mechanical efficiency for the optimal solution

$$\epsilon_W = \frac{\mathcal{W}_{\min}}{\mathcal{W}_{\text{opt}}} \leq 1, \quad [14]$$

which quantifies the extent to which energy is dissipated in internal modes rather than transporting the drop (Fig. 4D). Finally, we also use the coefficient of variation of the height—i.e., the ratio of the final displacement to size achieved by the drop,  $X(T)/R(T)$ , as a measure of transport precision (Fig. 4E, solid) and compare it against the prescribed value  $X_T/R_T$  for a given transport task (Fig. 4E, dashed). Interestingly, the optimal solutions for  $X_T/R_T = 0.2, 0.27$  achieve a higher precision (solid curves, Fig. 4E) than required by the task (dashed lines, Fig. 4E) across a large range of  $Ca_\zeta$ , but this enhanced performance degrades for larger  $X_T/R_T = 0.33, 0.4$ . As anticipated, all three performance metrics are nonmonotonic and display an optimal trade-off at intermediate values of  $Ca_\zeta$  (Fig. 4 C–E), with both the efficiency and the precision being maximized around  $Ca_\zeta \sim 100$  to 200, while the optimal cost is minimal at a slightly higher  $Ca_\zeta \sim 250$  to 380. Qualitatively similar trends appear as we vary the transport task via  $X_T/R_T$  (Fig. 4 C–E), though for larger values of  $X_T/R_T = 0.33, 0.4$  (in the infeasible region of the symmetric ODE optimal transport; Fig. 3C), the performance curves exhibit more kinks, perhaps suggestive of a rougher cost landscape with many nearly degenerate local minima when the task difficulty increases.

## Discussion

Complementing classical optimal transportation and its hydrodynamic analogies that use a very specific form of the cost (22), we have formulated a framework to address questions of optimal mass transport in physical continua obeying complex dynamical constraints and illustrated its utility in a simple, yet rich, problem of transporting a drop of an active suspension by dissipating the least amount of energy. Our strategy combines a finite-dimensional (ODE) description based on a physically motivated

mode-reduction scheme, along with the full infinite-dimensional (PDE) model, both of which we couch within optimal control theory to obtain a tractable and interpretable characterization of the resulting optimal transport policies. An important outcome is the prediction of intuitive gather–move–spread-style strategies and simple trade-offs between active and passive forces that emerge naturally within our formulation of optimal drop transport, with implications for a wide range of synthetic and living active matter.

In active physical systems, magnetically controlled ferrofluid drops (42–44), digital microfluidic platforms (45), and bi-component volatile liquids (46) might provide an immediate platform to deploy our framework. As an example, for ferrofluid droplets, the active stress would be replaced by a magnetic stress given by  $\sigma^m \approx \mu_0 M_s H$ , where  $\mu_0 = 4\pi \times 10^{-7}$  N/A<sup>2</sup> is the vacuum permeability,  $M_s \sim 10^4$  A/m is the ferrofluid saturation magnetization, and  $H \sim 10^3$  to  $10^4$  A/m is the magnetic field strength. Dimensional considerations suggest that small drops (size  $R \sim 1$  to 3 mm and height  $h \sim 1$  mm) with a typical viscosity  $\eta \sim 0.4$  Pa·s and surface tension  $\gamma \sim 10^{-2}$  N/m can easily achieve rapid movement with speeds  $\sim 0.1$  to 1 mm/s (42–44) and also change shape by varying the magnetic capillary number  $Ca_m \sim \sigma^m R^2 / \gamma h \sim 10$  to 100.

In bio-hybrid contexts, our work is directly relevant to the control of self-propelled drops composed of microtubule-kinesin nematic gels (4), swimming bacteria (47), and isolated motile cells (48, 49) that are often viewed as active drops (25, 33, 50, 51). Our results could also be tested by using optogenetically controlled living motile cells (52) or in reconstituted active drops (4, 53). Since the cortical tension of individual cells varies in the range of  $\gamma \sim 0.1$  to 1 mN/m (54) and the characteristic active stress  $\zeta h \sim 1$  kPa (50),  $Ca_\zeta \sim 10^2$  to  $10^3$  for a  $R = 10$  μm size cell (assuming an average height  $h \sim 1$  μm), allowing for an exploration of the transport cost versus internal dissipation trade-off at intermediate  $Ca_\zeta \sim \mathcal{O}(100)$  that we have uncovered here. This suggests that contractility driven cellular motility may be optimal, even beyond steady translation (30), by harnessing dynamic optimal protocols and internally regulating differential contractility against surface tension. Extensions of our framework can also easily be used to address the control and patterning of localized structures, such as defects in active fluids, which has been the focus of much research in recent years (13, 14, 55, 56).

More broadly, beyond the control of active systems, our formulation of optimal transport offers an alternative choice of transport metrics that are physically motivated and potentially richer than the conventional ones (like the  $L^2$ -Wasserstein norm) used in standard optimal transport (20), yet their mathematical properties remain to be uncovered. A tantalizing possibility is to exploit thermodynamic analogies connecting minimum dissipation protocols in stochastic systems to optimal transport (57). In this regard, a generalization of our framework to include fluctuations within stochastic optimal control (58) would be a promising future direction.

**Data, Materials, and Software Availability.** All study data are included in the article and/or supporting information.

**ACKNOWLEDGMENTS.** We acknowledge partial financial support from the Harvard Society of Fellows (S.S.), Harvard Materials Research Science and Engineering Center Grant DMR-2011754 (to L.M.), the NSF Simons Center for Mathematics and Complex Biological Systems Grant DMR-1764269 (to L.M.), the Simons Foundation (L.M.), and the Henri Seydoux Fund (L.M.); and we gratefully acknowledge illuminating discussions during the virtual 2020 Kavli Institute for Theoretical Physics program on “Symmetry, Thermodynamics and Topology in Active Matter,” which was supported in part by NSF Grant NSF PHY-1748958.

1. D. Needleman, Z. Dogic, Active matter at the interface between materials science and cell biology. *Nat. Rev. Mater.* **2**, 1–14 (2017).
2. R. Zhang, A. Mozaffari, J. J. de Pablo, Autonomous materials systems from active liquid crystals. *Nat. Rev. Mater.* **6**, 437–453 (2021).
3. S. Shankar, A. Souslov, M. J. Bowick, M. C. Marchetti, V. Vitelli, Topological active matter. *Nat. Rev. Phys.* **4**, 380–398 (2022).
4. T. Sanchez, D. T. Chen, S. J. DeCamp, M. Heymann, Z. Dogic, Spontaneous motion in hierarchically assembled active matter. *Nature* **491**, 431–434 (2012).
5. A. Bricard, J. B. Caussin, N. Desreumaux, O. Dauchot, D. Bartolo, Emergence of macroscopic directed motion in populations of motile colloids. *Nature* **503**, 95–98 (2013).
6. S. Zhou, A. Sokolov, O. D. Lavrentovich, I. S. Aranson, Living liquid crystals. *Proc. Natl. Acad. Sci. U.S.A.* **111**, 1265–1270 (2014).
7. G. Duclos *et al.*, Spontaneous shear flow in confined cellular nematics. *Nat. Phys.* **14**, 728–732 (2018).
8. M. C. Marchetti *et al.*, Hydrodynamics of soft active matter. *Rev. Mod. Phys.* **85**, 1143 (2013).
9. G. Viznyiczai *et al.*, Light controlled 3D micromotors powered by bacteria. *Nat. Commun.* **8**, 15974 (2017).
10. S. Krishnamurthy, S. Ghosh, D. Chatterji, R. Ganapathy, A. Sood, A micrometre-sized heat engine operating between bacterial reservoirs. *Nat. Phys.* **12**, 1134–1138 (2016).
11. J. Arlt, V. A. Martinez, A. Dawson, T. Pilizota, W. C. K. Poon, Painting with light-powered bacteria. *Nat. Commun.* **9**, 768 (2018).
12. G. Frangipane *et al.*, Dynamic density shaping of photokinetic *E. coli*. *eLife* **7**, e36608 (2018).
13. T. D. Ross *et al.*, Controlling organization and forces in active matter through optically defined boundaries. *Nature* **572**, 224–229 (2019).
14. R. Zhang *et al.*, Spatiotemporal control of liquid crystal structure and dynamics through activity patterning. *Nat. Mater.* **20**, 875–882 (2021).
15. T. Turiv *et al.*, Topology control of human fibroblast cells monolayer by liquid crystal elastomer. *Sci. Adv.* **6**, eaaz6485 (2020).
16. K. D. Endresen, M. Kim, M. Pittman, Y. Chen, F. Serra, Topological defects of integer charge in cell monolayers. *Soft Matter* **17**, 5878–5887 (2021).
17. D. J. Cohen, W. J. Nelson, M. M. Maharbiz, Galvanotactic control of collective cell migration in epithelial monolayers. *Nat. Mater.* **13**, 409–417 (2014).
18. T. J. Zajdel, G. Shim, L. Wang, A. Rossello-Martinez, D. J. Cohen, Scheepdog: Programming electric cues to dynamically herd large-scale cell migration. *Cell Syst.* **10**, 506–514.e3 (2020).
19. G. Monge, “Mémoire sur la théorie des déblais et des remblais.” in *Histoire de l’Académie Royale des Sci. de Paris*, J. Boudot, Ed. (De l’Imprimerie Royale, Paris, 1781), pp. 666–704.
20. C. Villani, *Optimal Transport: Old and New* (Grundlehren der Mathematischen Wissenschaften, Springer Science & Business Media, Berlin, 2008), vol. 338.
21. L. V. Kantorovich, On the translocation of masses in *Dokl. Akad. Nauk. USSR (NS)*. vol. 37, pp. 199–201 (1942) English translation. *J. Math. Sci.* **133**, 1381–1382 (2006).
22. J. D. Benamou, Y. Brenier, A computational fluid mechanics solution to the Monge-Kantorovich mass transfer problem. *Numer. Math.* **84**, 375–393 (2000).
23. J. F. Joanny, S. Ramaswamy, A drop of active matter. *J. Fluid Mech.* **705**, 46–57 (2012).
24. A. Loisy, J. Eggers, T. B. Liverpool, Tractionless self-propulsion of active drops. *Phys. Rev. Lett.* **123**, 248006 (2019).
25. A. Loisy, J. Eggers, T. B. Liverpool, How many ways a cell can move: The modes of self-propulsion of an active drop. *Soft Matter* **16**, 3106–3124 (2020).
26. R. Aditi Simha, S. Ramaswamy, Hydrodynamic fluctuations and instabilities in ordered suspensions of self-propelled particles. *Phys. Rev. Lett.* **89**, 058101 (2002).
27. P. G. De Gennes, Wetting: Statics and dynamics. *Rev. Mod. Phys.* **57**, 827 (1985).
28. P. G. De Gennes, F. Brochard-Wyart, D. Quéré, *Capillarity and Wetting Phenomena: Drops, Bubbles, Pearls, Waves* (Springer Science & Business Media, New York, 2013).
29. P. Pietzonka, É. Fodor, C. Lohrmann, M. E. Cates, U. Seifert, Autonomous engines driven by active matter: Energetics and design principles. *Phys. Rev. X* **9**, 041032 (2019).
30. P. Recho, J. F. Joanny, L. Truskinovsky, Optimality of contraction-driven crawling. *Phys. Rev. Lett.* **112**, 218101 (2014).
31. D. Liberzon, *Calculus of Variations and Optimal Control Theory: A Concise Introduction* (Princeton University Press, Princeton, NJ, 2011).
32. N. Hansen, “The CMA evolution strategy: A comparing review” in *Towards a New Evolutionary Computation*, J. A. Lozano, P. Larrañaga, I. Inza, E. Bengoetxea, Eds. (Studies in Fuzziness and Soft Computing, Springer Berlin Heidelberg, Berlin), vol. 192, pp. 75–102 (2006).
33. P. Recho, T. Putelat, L. Truskinovsky, Contraction-driven cell motility. *Phys. Rev. Lett.* **111**, 108102 (2013).
34. R. W. Brockett, Nonlinear systems and differential geometry. *Proc. IEEE* **64**, 61–72 (1976).
35. R. Hermann, A. Krener, Nonlinear controllability and observability. *IEEE Trans. Automat. Contr.* **22**, 728–740 (1977).
36. L. Pontryagin, *Mathematical Theory of Optimal Processes* (CRC Press, Boca Raton, FL, 1987).
37. J. A. Andersson, J. Gillis, G. Horn, J. B. Rawlings, M. Diehl, CasADi: A software framework for nonlinear optimization and optimal control. *Math. Program. Comput.* **11**, 1–36 (2019).
38. R. W. Brockett, “Minimum attention control” in *Proceedings of the 36th IEEE Conference on Decision and Control* (IEEE, Piscataway, NJ, 1997), vol. 3, pp. 2628–2632.
39. M. Alnaes, *et al.*, The FEniCS project version 1.5. *Arch. Numer. Softw.*, 10.11588/ans.2015.100.20553 (2015).
40. A. Logg, K. A. Mardal, G. Wells, *Automated Solution of Differential Equations by the Finite Element Method: The FEniCS Book* (Lecture Notes in Computational Science and Engineering, Springer Science & Business Media, Berlin, 2012), vol. 84.
41. A. Lacey, J. Ockendon, A. Tayler, “Waiting-time” solutions of a nonlinear diffusion equation. *SIAM J. Appl. Math.* **42**, 1252–1264 (1982).
42. N. T. Nguyen, K. M. Ng, X. Huang, Manipulation of ferrofluid droplets using planar coils. *Appl. Phys. Lett.* **89**, 052509 (2006).
43. R. Probst *et al.*, Planar steering of a single ferrofluid drop by optimal minimum power dynamic feedback control of four electromagnets at a distance. *J. Magn. Magn. Mater.* **323**, 885–896 (2011).
44. K. S. Khalil, S. R. Mahmoudi, N. Abu-Dheir, K. K. Varanasi, Active surfaces: Ferrofluid-impregnated surfaces for active manipulation of droplets. *Appl. Phys. Lett.* **105**, 041604 (2014).
45. R. B. Fair, Digital microfluidics: Is a true lab-on-a-chip possible? *Microfluid. Nanofluidics* **3**, 245–281 (2007).
46. N. J. Ciria, A. Benusiglio, M. Prakash, Vapour-mediated sensing and motility in two-component droplets. *Nature* **519**, 446–450 (2015).
47. M. Rajabi, H. Baza, T. Turiv, O. D. Lavrentovich, Directional self-locomotion of active droplets enabled by nematic environment. *Nat. Phys.* **17**, 260–266 (2021).
48. K. Keren *et al.*, Mechanism of shape determination in motile cells. *Nature* **453**, 475–480 (2008).
49. D. B. Brückner *et al.*, Stochastic nonlinear dynamics of confined cell migration in two-state systems. *Nat. Phys.* **15**, 595–601 (2019).
50. K. Kruse, J. F. Joanny, F. Jülicher, J. Prost, Contractility and retrograde flow in lamellipodium motion. *Phys. Biol.* **3**, 130–137 (2006).
51. E. Tjhung, A. Tiribocchi, D. Marenduzzo, M. E. Cates, A minimal physical model captures the shapes of crawling cells. *Nat. Commun.* **6**, 5420 (2015).
52. Y. I. Wu *et al.*, A genetically encoded photoactivatable Rac controls the motility of living cells. *Nature* **461**, 104–108 (2009).
53. H. Boukellal, O. Campàs, J. F. Joanny, J. Prost, C. Sykes, Soft Listeria: Actin-based propulsion of liquid drops. *Phys. Rev. E Stat. Nonlin. Soft Matter Phys.* **69**, 061906 (2004).
54. G. Salbreux, G. Charas, E. Paluch, Actin cortex mechanics and cellular morphogenesis. *Trends Cell Biol.* **22**, 536–545 (2012).
55. S. Shankar, M. C. Marchetti, Hydrodynamics of active defects: From order to chaos to defect ordering. *Phys. Rev. X* **9**, 041047 (2019).
56. M. M. Norton, P. Grover, M. F. Hagan, S. Fraden, Optimal control of active nematics. *Phys. Rev. Lett.* **125**, 178005 (2020).
57. E. Aurell, C. Mejía-Monasterio, P. Muratore-Ginanneschi, Optimal protocols and optimal transport in stochastic thermodynamics. *Phys. Rev. Lett.* **106**, 250601 (2011).
58. Y. Chen, T. T. Georgiou, M. Pavon, Optimal transport in systems and control. *Annu. Rev. Control. Robot. Auton. Syst.* **4**, 89–113 (2020).

1

## 2 **Supplementary Information for** 3 **Optimal transport and control of active drops**

4 **Suraj Shankar, Vidya Raju, and L. Mahadevan**

5 **Correspondence and requests for materials should be addressed to L. Mahadevan.**  
6 **E-mail: [lmahadev@g.harvard.edu](mailto:lmahadev@g.harvard.edu)**

### 7 **This PDF file includes:**

- 8     Supplementary text
- 9     Figs. S1 to S3
- 10    Legends for Movies S1 to S3
- 11    SI References

### 12 **Other supplementary materials for this manuscript include the following:**

- 13     Movies S1 to S3

## 14 Supporting Information Text

### 15 1. Controllability and finite dimensional optimal control

16 We briefly outline the relevant control theoretic notions that allow us to formulate and solve the ODE formulation of the  
 17 optimal transport problem. Consider a general dynamical system evolving on a smooth  $n$ -dimensional manifold  $\mathcal{M}$  (the state  
 18 space), of the form

$$19 \quad \dot{y}(t) = f_0(y(t)) + \sum_{i=1}^m u_i(t) f_i(y(t)), \quad [S1]$$

20 where  $u_i(t)$ ,  $i = 1, \dots, m$  are the control variables,  $f_0(y)$  is a drift vector field, and  $V(y) = \{f_i(y) \in T_y\mathcal{M}, i = 1, \dots, m\}$  is  
 21 the set of nonlinear control vector fields in the tangent space ( $T_y\mathcal{M}$ ) at a point  $y \in \mathcal{M}$ . This system is said to be *drift-free*  
 22 if  $f_0(y) = 0$ , and *underactuated* if there are fewer controls than the dimensionality of the manifold, i.e.,  $m < \dim(\mathcal{M}) = n$ .  
 23 When  $m < n$ , let  $\mathcal{V} = \cup_{y \in \mathcal{M}} \text{span}(V(y)) \subset T\mathcal{M}$  be the  $m$ -dimensional restricted sub-bundle within the tangent bundle  
 24  $T\mathcal{M} = \cup_{y \in \mathcal{M}} T_y\mathcal{M}$ . In the following, we limit our attention to drift-free systems and state sufficient conditions for the existence  
 25 of controls in this setting.

**Definition 1.1 (Controllability)** *Consider the drift-free dynamics*

$$26 \quad \dot{y}(t) = \sum_{i=1}^m u_i(t) f_i(y(t)) \quad [S2]$$

27 *evolving on a smooth  $n$ -dimensional manifold  $\mathcal{M}$ . This system is said to be controllable if there exist controls  $u_i$  that steer the  
 28 state from any initial configuration  $y_0 \in \mathcal{M}$  to any final configuration  $y_1 \in \mathcal{M}$ .*

29 The definition of controllability stated here does not specify the duration required to achieve the state transfer. For the  
 30 special case of linear dynamical systems taking the form  $\dot{y} = Ay + Bu$ , controllability implies finite time controllability. In fact  
 31 for this dynamics, if a prescribed state transfer is possible, it is possible in arbitrarily small time (1). However, more general  
 32 systems such as S2 may be controllable, and yet not finite-time controllable.

33 For nonlinear dynamical systems such as in Eq. S2, the non-commutativity of the control vector fields (measured by the Lie  
 34 bracket) plays a crucial role in determining the controllability of Eq. S1.

**Definition 1.2 (Lie Bracket)** *For two vector fields  $f_i(y)$ ,  $f_j(y) \in V(y)$ , their Lie bracket is defined as*

$$35 \quad [f_i(y), f_j(y)] = \nabla_y f_j(y) f_i(y) - \nabla_y f_i(y) f_j(y). \quad [S3]$$

36 The Lie bracket dictates the tangent direction along which the dynamical system is steered under an infinitesimal cyclic  
 37 actuation of the respective modulating controls  $u_i$  and  $u_j$ . The Lie algebra generated by the vector fields in  $V(y)$ , denoted by  
 38  $\{f_i(y), 1 \leq i \leq m\}_{L.A.}$ , is constructed by equipping the vector space  $V(y)$  with the Lie bracket operation (Eq. S3).

39 The theorem of Chow-Rashevsky (2) then provides the sufficient condition for the dynamics to be controllable.

40 **Theorem 1.1 (Chow-Rashevsky theorem)** *Consider the dynamical system (S2) defined on a smooth manifold  $\mathcal{M}$  of  
 41 dimension  $n$ . This system is controllable if for all  $y \in \mathcal{M}$ , there exist  $n$  linearly independent vector fields in the Lie algebra  
 42  $\{f_i(y), 1 \leq i \leq m\}_{L.A.}$  generated by  $\{f_i\}_{i=1}^m$ , that span the tangent space  $T_y\mathcal{M}$ .*

43 Theorem 1.1 provides a test for the global notion of controllability that depends on a local quantity, the Lie bracket. For  
 44 dynamics with drift such as in Eq. S1, the ability to steer in any direction in the neighbourhood of a point in  $\mathcal{M}$  is restricted  
 45 by the drift vector field. Hence, in such cases, local notions of accessibility and controllability need to be considered, but we do  
 46 not discuss them here for simplicity (see Ref. (2) for a pedagogical introduction).

47 **A. Optimal control problem formulation.** Consider again a drift-free system (Eq. S2) on the smooth manifold  $\mathcal{M}$  ( $\dim(\mathcal{M}) = n$ ):

$$48 \quad \dot{y}(t) = \sum_{i=1}^m u_i(t) f_i(y(t)) \equiv \mathbf{\Omega}(y(t)) \mathbf{u}(t), \quad [S4]$$

49 where  $\mathbf{\Omega}(y) = [f_1(y) \cdots f_m(y)]$ , and  $\mathbf{u}(t) = [u_1(t) \cdots u_m(t)]^T$ . Suppose that our goal is to steer the state from  $y(0)$  to  $y(T)$   
 50 in finite time  $T$ , along a trajectory governed by Eq. S2, while minimizing the cost functional  $\mathcal{C}$

$$51 \quad \mathcal{C} = \int_0^T dt \mathcal{L}(t, y, \mathbf{u}). \quad [S5]$$

52 In general, the Lagrangian  $\mathcal{L}$  can depend on the state ( $y$ ), the controls ( $\mathbf{u}$ ), but also on time ( $t$ ). In the simplest setting, the  
 53 Lagrangian involves a quadratic form  $\mathcal{L} = \mathbf{u}^T \mathbf{M}(y) \mathbf{u}$  with a state dependent positive semi-definite matrix  $\mathbf{M}(y)$ . Furthermore,  
 54 if the controls entering  $\mathcal{L}$  can be related to and eliminated in favour of the state dynamics (using Eq. S4), then the cost function  
 55 takes the form

$$56 \quad \mathcal{C} = \int_0^T dt \dot{y}(t)^T g(y(t)) \dot{y}(t), \quad [S6]$$

57 where  $g(y)$  is a symmetric matrix, which when nondegenerate and positive definite, endows the manifold  $\mathcal{M}$  with a metric  
58 tensor. In the case when  $m = n$  and  $\mathbf{\Omega}(y)$  has full rank (so is invertible),  $g(y) = [\mathbf{\Omega}(y)^{-1}]^T \mathbf{M}(y) \mathbf{\Omega}(y)$  is an  $n \times n$  symmetric  
59 matrix that provides a Riemannian metric (when nondegenerate) on  $\mathcal{M}$ . For  $m < n$ , the dynamics in Eq. S4 may still admit a  
60 rewriting of the cost as Eq. S6, with  $g(y)$  now being an  $m \times m$  symmetric positive definite matrix that defines a *sub-Riemannian*  
61 metric on the distribution  $\mathcal{V} \subset T\mathcal{M}$  instead (3, 4). In either case, the problem of finding optimal solutions for the steering the  
62 state then reduces to a geometric problem, one of finding a minimizing geodesic connecting the desired initial and final states,  
63 with the appropriate metric  $g(y)$  induced by the Lagrangian.

64 If Eq. S4 is controllable, then there exists a solution to the state transfer problem. With this assumption, we can use  
65 variational calculus to write down the first order necessary conditions for optimality of the controls, which we discuss below.

66 **B. Pontryagin Maximum Principle.** For a controllable dynamical system of the form in Eq. S4, Pontryagin's Maximum Principle  
67 (5, 6) prescribes the first order necessary conditions for optimality.

**Theorem 1.2 (Pontryagin's Maximum Principle (PMP))** *Suppose there exist optimal controls  $\mathbf{u}^*(t) = [u_1^*(t) \cdots u_m^*(t)]^T$  that minimize the cost  $\mathcal{C}$  in Eq. S5 along trajectories satisfying Eq. S4, and the corresponding optimal state trajectory is denoted as  $\mathbf{y}^*(t)$ . Then, there exists a costate trajectory  $\mathbf{p}(t)$  such that*

$$\dot{\mathbf{y}}^* = \partial_{\mathbf{p}} H(t, \mathbf{y}^*, \mathbf{p}, \mathbf{u}^*), \quad [\text{S7}]$$

$$\dot{\mathbf{p}} = -\partial_{\mathbf{y}^*} H(t, \mathbf{y}^*, \mathbf{p}, \mathbf{u}^*), \quad [\text{S8}]$$

68 where the Hamiltonian,

$$H(t, \mathbf{y}, \mathbf{p}, \mathbf{u}^*) = \max_{\mathbf{u}} \mathcal{H}(t, \mathbf{y}, \mathbf{p}, \mathbf{u}), \quad [\text{S9}]$$

69 is defined as the maximum of the pre-Hamiltonian  $\mathcal{H}$  over the controls. For the cost in Eq. S5, the pre-Hamiltonian is defined as

$$\mathcal{H}(t, \mathbf{y}, \mathbf{p}, \mathbf{u}) = \mathbf{p}^T \mathbf{\Omega}(y) \mathbf{u} - \mathcal{L}(t, \mathbf{y}, \mathbf{u}). \quad [\text{S10}]$$

72 If the system (Eq. S2) is controllable with  $m < n$ , and the quadratic cost  $\mathcal{C}$  can be written in terms of a positive definite  
73 metric  $g$  (Eq. S6), then we have an optimal control problem with a sub-Riemannian metric endowed by the cost on the  
74  $m$ -dimensional distribution  $\mathcal{V}$  spanned by the set of control vector fields. This is called a sub-Riemannian optimal control  
75 problem (4).

## 76 2. Reduced order dynamics and ODE drop control

77 Here we provide the details of the Galerkin projection calculation to obtain the finite dimensional ODE model of drop dynamics  
78 from the continuum equations. We also derive the optimal control solution for the two parameter  $(X, R)$  description of drop  
79 transport, extend the parametrization to account for drop shape and discuss the associated optimal control problem. In  
80 addition to providing a finite dimensional representation, this formulation is also ripe for the direct application of results from  
81 optimal control theory to check feasibility as well as provide, to the extent possible, analytical expressions for the transport  
82 plan.

83 **A. Two parameter model reduction.** The continuum dynamics of the drop is given by a continuity equation for the drop height  
84  $h(x, t)$  ( $\int dx h = 1$ )

$$\partial_t h + \partial_x q = 0, \quad q = \frac{h^3}{3\eta} \partial_x (\zeta h + \gamma \partial_x^2 h), \quad [\text{S11}]$$

86 driven by spatiotemporally varying activity  $\zeta(x, t)$  and a constant surface tension  $\gamma$ . As described in the main text, in the  
87 absence of activity ( $\zeta = 0$ ), the flux vanishes when  $\partial_x^3 h = 0$ , i.e.,  $h(x, t)$  is parabolic,

$$h(x, t) = \frac{6}{R(t)^3} \left[ \frac{R(t)^2}{4} - (x - X(t))^2 \right], \quad [\text{S12}]$$

89 and is parametrized by its position  $X(t) = \int dx x h(x, t)$  and its size  $R(t) = \sqrt{20\Delta(t)}$  (which is related as to the variance  
90  $\Delta(t) = \int dx (x - X(t))^2 h(x, t)$ ). In order to obtain the effective dynamics of the drop in terms of  $\dot{X}$  and  $\dot{R}$ , we take moments  
91 of Eq. S11 to get

$$\dot{X}(t) = \int_{X(t)-R(t)/2}^{X(t)+R(t)/2} dx q(x, t), \quad \dot{R}(t) = \int_{X(t)-R(t)/2}^{X(t)+R(t)/2} dx (x - X(t)) q(x, t). \quad [\text{S13}]$$

93 The limits  $X(t) \pm R(t)/2$  are simply the ends of the drop, beyond which  $h = 0$ . This provides a closed system of equations to  
94 describe drop dynamics on the parametrized manifold invariant to surface tension flows, upon which the controlled dynamics  
95 steered by activity occurs.

96 **B. Two dimensional ODE optimal control.** Upon evaluating Eq. S13 along with the activity parametrization (Eq. 4, main text),  
 97 we obtain the drop position and size dynamics to be

$$98 \quad \dot{X}(t) = \frac{18\Delta\zeta(t)}{35\eta R(t)^4}, \quad \dot{R}(t) = -\frac{24\zeta_0(t)}{7\eta R(t)^4}. \quad [S14]$$

99 As expected, the mean and gradient components of the active stress independently control the drop size and position respectively.  
 100 This, together with non-vanishing control vector fields for finite  $R$ , trivially ensure controllability. For simplicity, we shall  
 101 consider the fixed end point problem, in which case the cost  $\mathcal{C} = \mathcal{W}$  is simply the net dissipation,  $\mathcal{W} = \int_0^T dt \mathcal{L}$ , where the  
 102 Lagrangian is  $\mathcal{L} = (1/\eta R^6)[(72/35)\zeta_0^2 + (54/77)\Delta\zeta^2]$ . The Lagrangian is simply quadratic in the controls  $(\zeta, \Delta\zeta)$ , and has  
 103 a strong size dependence due to the nonlinear dependence of the dissipation and friction on the height of the drop. Upon  
 104 denoting the state vector as  $\Psi(t) = [X(t) R(t)]^T$  and the costate (Lagrange multipliers) as  $p(t) = [p_X(t) p_R(t)]^T$  to enforce  
 105 the dynamical constraints in Eq. S14, a necessary condition for optimality is given by PMP. We then maximize the control  
 106 Hamiltonian

$$107 \quad \mathcal{H}(\Psi, p, \zeta_0, \Delta\zeta) = p_X \frac{18\Delta\zeta}{35\eta R^4} - p_R \frac{24\zeta_0}{7\eta R^4} - \mathcal{L}, \quad [S15]$$

108 over the controls to get  $\zeta_0^* = -5p_R R^2/6$  and  $\Delta\zeta^* = 11p_X R^2/30$  as the maximizers. When plugged back into Eq. S15, this  
 109 gives the conserved Hamiltonian (as it doesn't depend explicitly on time)

$$110 \quad H(\Psi, p) \equiv \mathcal{H}(\Psi, p, \zeta_0^*, \Delta\zeta^*) = \frac{1}{7\eta R^2} \left( 10p_R^2 + \frac{33}{50}p_X^2 \right). \quad [S16]$$

111 The candidate extremals for the optimal control problem are now obtained as solutions to the following Hamiltonian dynamics

$$112 \quad \dot{\Psi} = \frac{\partial H}{\partial p}, \quad \dot{p} = -\frac{\partial H}{\partial \Psi}. \quad [S17]$$

113 For the state variables  $\Psi(t)$ , this gives back Eq. S14 driven by the optimal controls  $(\zeta_0^*(t), \Delta\zeta^*(t))$ . Translational invariance  
 114 enforces that  $\partial_X \mathcal{H} = 0$ , hence  $p_X$  is also conserved along the optimal trajectory.

115 To obtain analytical expressions for the costate and optimal activity, we reparametrize time to linearize the dynamics. We  
 116 define  $\tau(t)$  so that

$$117 \quad \dot{\tau} = \frac{1}{\eta R^2}, \quad [S18]$$

118 with the initial condition  $\tau(0) = 0$ . Upon writing  $\chi(\tau) = X(t)$ ,  $\rho(\tau) = R(t)$ ,  $P(\tau) = p_R(t)$  and  $p_X = p_0$  (a constant), we obtain  
 119 (primes denote d/d $\tau$ )

$$120 \quad \chi' = \frac{33}{175}p_0, \quad \rho' = \frac{20}{7}P, \quad P' = 2\eta\rho H_0, \quad [S19]$$

121 where  $H_0$  (constant) is the conserved value of the Hamiltonian along the optimal solution. The position equation can be  
 122 integrated trivially to give  $\chi(\tau) = (33p_0/175)\tau$  and the last two equations can be combined to give a linear equation for  $\rho(\tau)$ ,

$$123 \quad \rho'' - \kappa^2\rho = 0 \implies \rho(\tau) = \frac{R_T \sinh(\kappa\tau) + R_0 \sinh[\kappa(\tau(T) - \tau)]}{\sinh[\kappa\tau(T)]}, \quad [S20]$$

124 where we have used the boundary conditions on the drop size ( $R(0) = R_0$ ,  $R(T) = R_T$ ) and defined the (as of yet) undetermined  
 125 constant

$$126 \quad \kappa^2 = \frac{40\eta}{7}H_0. \quad [S21]$$

127 By imposing the boundary condition on the drop position, we obtain

$$128 \quad X_T = \frac{33}{175}p_0\tau(T). \quad [S22]$$

129 To compute the value of  $\kappa$  and  $p_0$ , we evaluate the conserved Hamiltonian at  $t = 0$  to get

$$130 \quad H_0 = \frac{1}{7\eta R_0^2} \left[ 10p_R(0)^2 + \frac{33}{50}p_0^2 \right], \quad [S23]$$

131 in which we can plug in the value of  $p_R(0) \equiv P(0) = (7/20)\rho'(0) = (7\kappa/20 \sinh[\kappa\tau(T)])\{R_T - R_0 \cosh[\kappa\tau(T)]\}$  along with the  
 132 expression for  $p_0$  (from Eq. S22) to get

$$133 \quad \frac{X_T}{R_0} = \sqrt{\frac{33s^2}{500 \sinh^2 s} \left[ \left( \frac{R_T}{R_0} \right) \left( 2 \cosh s - \frac{R_T}{R_0} \right) - 1 \right]} \equiv \mathcal{F} \left( s, \frac{R_T}{R_0} \right), \quad [S24]$$

134 where  $s = \kappa\tau(T) > 0$  is the unknown to be solved for. Remarkably, this equation lacks any real solution for  $s > 0$  if  $X_T/R_0$  is  
 135 sufficiently large for a given ratio  $R_T/R_0$ . One can show that Eq. S24 in general has either two positive solutions, one positive  
 136 solution or none. By using the locus of coinciding solutions, we can compute the envelope curve of the maximal displacement  
 137 for a given size change, above which Eq. S24 has no real solutions. This determines the feasibility curve for smooth optimal

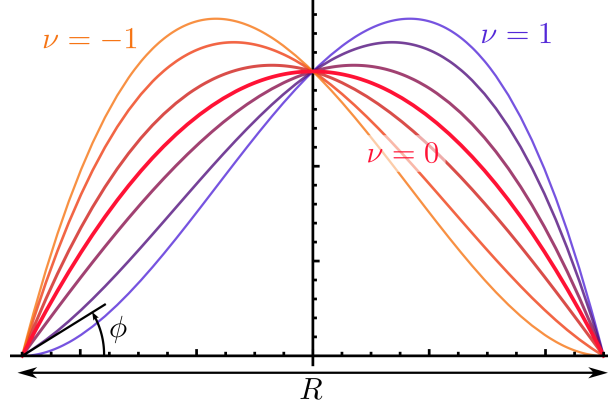


**Fig. S1.** The parametrization of the drop height (Eq. S27) in terms of its position ( $X$ , here centered to the origin), size ( $R$ ) and an asymmetry ( $\nu$ ) that captures a tilt in the drop profile. For  $\nu = 0$ , we have a symmetric parabolic drop, and for  $\nu = \pm 1$  (the extremes), we have a right or left leaning drop respectively. The asymmetry  $\nu$  is related to the trailing (left most) contact angle  $\phi$  of the drop, via  $\nu = 1 - (R^2\phi/6)$ .

138 policies (at least  $C^2$  regularity) which is shown in Fig. 3C (main text). For large size disparities  $R_T/R_0 \rightarrow \infty$ , we can compute  
 139 the asymptotic behaviour of this bounding curve to be a weak logarithm,

$$140 \quad \left(\frac{X_T}{R_0}\right)_{\max} \simeq \sqrt{\frac{33}{500}} \ln\left(\frac{2R_T}{R_0}\right) \quad \left(\frac{R_T}{R_0} \rightarrow \infty\right). \quad [\text{S25}]$$

141 By solving Eq. S24 numerically for  $s = \kappa\tau(T)$ , when it exists, we can use the final relation between  $\tau(T)$  and  $T$  (by integrating  
 142 Eq. S18) to get

$$143 \quad \frac{\tau(T)}{4s \sinh^2 s} [(R_0^2 + R_T^2)(\sinh(2s) - 2s) + 4R_0R_T(s \cosh s - \sinh s)] = \frac{T}{\eta}. \quad [\text{S26}]$$

144 This directly gives  $\tau(T)$  and hence  $\kappa$  (by using the now known value of  $s$ ) and also  $H_0$ , thereby completing the full solution.  
 145 Representative curves for the control and state dynamics are plotted in Fig. 2A-B, main text.

146 **C. Three parameter model reduction.** Here we extend our previous calculation to include a third variable that captures changes  
 147 in drop shape, in addition to position and size. We parametrize the shape of the drop using a cubic polynomial that additionally  
 148 captures the drop asymmetry, i.e., a tilting of the drop (see Fig. S1). Upon using  $\int dx h = 1$ , we obtain

$$149 \quad h(x, t) = \frac{12\nu(t)}{R(t)^4} (x - a(t))(a(t) + R(t) - x) \left[ x - a(t) + \frac{R(t)(1 - \nu(t))}{2\nu(t)} \right], \quad [\text{S27}]$$

where  $a(t) = X(t) - (R(t)/2) - R(t)\nu(t)/10$  is the trailing (left most) end of the drop and the dimensionless asymmetry  
 $\nu \in [-1, 1]$  is related to the trailing (left most) contact angle  $\phi(t)$  of a right moving drop via  $\nu(t) = 1 - R(t)^2\phi(t)/6$  (see  
 Fig. S1). Note that  $h = 0$  at the two ends of the drop,  $x = a$  and  $x = a + R$ , and vanishes outside this region. The drop  
 asymmetry is restricted to the interval  $\nu \in [-1, 1]$  to ensure the height in Eq. S27 is always positive. While the extreme limits  
 of  $\nu = \pm 1$  correspond to a right and left leaning drop respectively (Fig. S1), for  $\nu = 0$ , the drop has a symmetric parabolic  
 profile. The position  $X = \int dx xh$  is still directly given by the mean, while the size  $R(t)$  and asymmetry  $\nu(t)$  of the drop can  
 be related to the next two spatial moments of the height field  $h(x, t)$  via

$$\Delta = \int dx (x - X)^2 h = \frac{R^2}{100} [5 - \nu^2], \quad [\text{S28}]$$

$$\Phi = \int dx (x - X)^3 h = \frac{R^3}{3500} \nu [7\nu^2 - 15]. \quad [\text{S29}]$$

We can similarly compute spatial moments of the flux  $q(x, t)$  to obtain

$$\dot{X}(t) = \int_{a(t)}^{a(t)+R(t)} dx q(x, t), \quad [\text{S30}]$$

$$\dot{\Delta}(t) = 2 \int_{a(t)}^{a(t)+R(t)} dx (x - X(t)) q(x, t), \quad [\text{S31}]$$

$$\dot{\Phi}(t) = 3 \int_{a(t)}^{a(t)+R(t)} dx [(x - X(t))^2 - \Delta(t)] q(x, t). \quad [\text{S32}]$$

150 These equations can be inverted using Eqs. S28, S29 to obtain the complete and closed set of nonlinear dynamical equations  
 151 governing the evolution of the drop position  $X(t)$ , size  $R(t)$  and tilt  $\nu(t)$ . If we set  $\nu = 0$  by fiat and neglect  $\dot{\nu}$ , then we recover

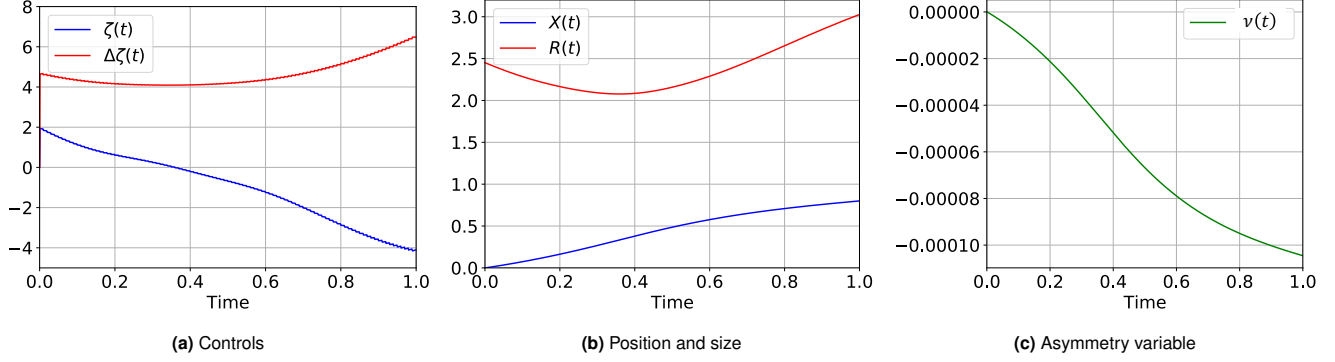


**Fig. S2.** Solution to the three dimensional ODE optimal control problem with the asymmetry variable ( $\nu(t)$ ) forced to be close to zero (when  $\lambda = 10^5$ ) recovers the gather-move-spread strategy. The optimal control problem was solved using CasADi (7) with time step  $dt = 10^{-3}$ . The final position was imposed as a hard terminal constraint, while the size constraint was imposed by a quadratic terminal cost with  $\mu_R = 9 \times 10^{-6}$ .

152 the coupled  $(X, R)$  dynamics given in Eq. S14. Note that, the low order Galerkin approximation employed here works best in  
 153 the bulk of the drop and cannot capture boundary phenomena that occur close to the contact line. While the symmetric drop  
 154 parametrized by just  $X, R$  (Eq. S12) corresponds to an effective zero mode of capillary forces (atleast within the bulk of the  
 155 drop, size change is affected by  $\gamma$  when the contact angle and boundary effects are taken into account), in the presence of drop  
 156 asymmetry ( $\nu \neq 0$ ), this is no longer the case and surface tension forces will be present even in the bulk of the drop. In order  
 157 to avoid complications from surface tension and wetting related boundary effects, we set  $\gamma = 0$  for simplicity here and consider  
 158 only the high active capillary number limit ( $Ca_\zeta \gg 1$ ).

159 **D. Three dimensional ODE optimal control.** The configuration space of the drop is now characterized by a three dimensional  
 160 manifold  $\mathcal{M}$  comprising the state variables  $X, R$  and  $\nu$ . We denote the state by a column vector  $\Psi(t) = [X(t) R(t) \nu(t)]^T$   
 161 evolving in  $\mathcal{M} = \mathbb{R} \times \mathbb{R}^+ \times [-1, 1]$ , whose dynamics constitutes a time-invariant, drift-free, and underactuated nonlinear  
 162 dynamical system, given by

$$\dot{\Psi}(t) = \zeta_0(t)F(\Psi(t)) + \Delta\zeta(t)G(\Psi(t)), \quad [\text{S33}]$$

where  $F(\Psi)$ ,  $G(\Psi)$  are nonlinear control vector fields, constituting two tangent directions that are independently controlled by  
 the mean and gradient components of the activity

$$F(\Psi) = \frac{1}{\eta R^4} \begin{bmatrix} 0 \\ F_R \\ F_\nu \\ R \end{bmatrix} = \frac{1}{\eta R^4} \begin{bmatrix} 0 \\ \frac{24[224 - (1 - \nu^2)(448 - 81(1 - \nu^2))]}{1001(1 - \nu^2)} \\ \frac{1}{\lambda R} \frac{768\nu[28 + (1 - \nu^2)(14 - 3(1 - \nu^2))]}{1001(1 - \nu^2)} \\ R \end{bmatrix}, \quad [\text{S34}]$$

$$G(\Psi) = \frac{1}{\eta R^4} \begin{bmatrix} G_X \\ G_R \\ G_\nu \\ R \end{bmatrix} = \frac{1}{\eta R^4} \begin{bmatrix} \frac{18}{5005} [224 - 3(1 - \nu^2)(28 - (1 - \nu^2))] \\ -\frac{12\nu[352 - (1 - \nu^2)(80 - (1 - \nu^2))]}{1001(1 - \nu^2)} \\ \frac{1}{\lambda R} \frac{24[704 + (1 - \nu^2)(32 - (1 - \nu^2)(104 - 5(1 - \nu^2)))]}{1001(1 - \nu^2)} \\ R \end{bmatrix}. \quad [\text{S35}]$$

164 Note that elements of  $F(\Psi)$  and  $G(\Psi)$  depend only on the size and asymmetry of the drop and are independent of its position,  
 165 as expected from translational invariance. Interestingly though,  $F$  doesn't contribute to  $\dot{X}$ , i.e., even when the drop is spatially  
 166 asymmetric ( $\nu \neq 0$ ), a mean activity ( $\zeta_0 \neq 0$ ) does not generate translation, although this is not prohibited by the Curie  
 167 principle (8). We have introduced an additional continuation parameter  $\lambda$  in the dynamics of  $\nu$  alone, that we tune from  
 168  $\lambda = \infty$  to  $\lambda = 1$  within a homotopy continuation scheme. In the  $\lambda = \infty$  limit, we recover the symmetric drop system for which  
 169 we have exact analytical optimal controls provided in Sec. B. Upon decreasing  $\lambda$  with concurrent numerical optimization using  
 170 CasADi (7), we progressively deform the known symmetric drop optimal solution into the required optimal policy for the three  
 171 parameter problem when  $\lambda = 1$ . As before, we assume the initial location of the drop is  $X_0 = 0$ , and initial size  $R_0 = \sqrt{6}$ . The  
 172 final position and size are also fixed to be  $X_T = 0.8$  and  $R_T = 3$ . While we impose a fixed end-point condition on the position  
 173 ( $X(T) = X_T$ ), we relax the terminal constraint on size with a finite cost  $\mu_R = 9 \times 10^{-6}$  and leave  $\nu(T)$  as a free, unconstrained  
 174 variable.

175 We verify controllability symbolically using Mathematica (9) by checking that  $\{F, G, [F, G]\}$  constitute a basis spanning the  
 176 tangent space everywhere in the drop configuration space,  $\text{int}(\mathcal{M}) = \mathbb{R} \times (0, \infty) \times (-1, 1)$ . Hence Eq. S33 is controllable and  
 177 presents an underactuated sub-Riemannian optimal control problem. This implies that there exist controls  $(\zeta_0, \Delta\zeta)$  that can  
 178 steer any state  $\Psi_1$  into any other state  $\Psi_2$  in the drop configuration space.

179 The net dissipation is once again  $\mathcal{W} = \int_0^T dt \mathcal{L}$ , with the Lagrangian

$$180 \quad \mathcal{L} = \frac{1}{\eta R^6} \mathbf{u}^T \mathbf{M} \mathbf{u}, \quad [\text{S36}]$$

where  $\mathbf{u} = [\zeta \ \Delta\zeta]^T$  and  $\mathbf{M}$  is a  $2 \times 2$  symmetric matrix with entries

$$M_{11}(\nu) = \frac{72}{385} [32 - 3(1 - \nu^2)(8 - (1 - \nu^2))], \quad [\text{S37}]$$

$$M_{12}(\nu) = -\frac{72}{10010} \nu [160 - 3(1 - \nu^2)(24 - (1 - \nu^2))], \quad [\text{S38}]$$

$$M_{22}(\nu) = \frac{18}{5005} [416 - (1 - \nu^2)(248 - 27(1 - \nu^2))]. \quad [\text{S39}]$$

One can easily check by explicit diagonalization that  $\mathbf{M}$  is always positive definite and nondegenerate ( $\det(\mathbf{M}) \neq 0$ ) for all  $\nu \in [-1, 1]$ . Compactly, the dynamics can be written as  $\dot{\Psi} = \mathbf{\Omega}(\Psi)\mathbf{u}$ , where

$$\begin{aligned} \mathbf{\Omega}(\Psi) &= [F \ G] \\ &= \frac{1}{\eta R^6} \begin{bmatrix} 0 & R^2 G_X \\ R^2 F_R & R^2 G_R \\ R F_\nu & R G_\nu \end{bmatrix}. \end{aligned} \quad [\text{S40}]$$

Further, let  $V_1 = R p_R F_R + p_\nu F_\nu$  and  $V_2 = R p_X G_X + R p_R G_R + p_\nu G_\nu$ , and  $\tilde{\mathbf{v}} = [V_1 \ V_2]^T$  so that  $\mathbf{w} = R\tilde{\mathbf{v}}$ . The pre-Hamiltonian  $\mathcal{H}(\Psi, p, \mathbf{u})$ , and the optimal control  $\mathbf{u}^*$  obtained by its maximization is given as

$$\mathcal{H}(\Psi, p, \mathbf{u}) = \frac{1}{\eta R^6} [\mathbf{w}^T \mathbf{u} - \mathbf{u}^T \mathbf{M} \mathbf{u}], \quad [\text{S41}]$$

$$\mathbf{u}^* = \frac{1}{2} \mathbf{M}^{-1} \mathbf{w}, \quad [\text{S42}]$$

181 so that the Hamiltonian is

$$182 \quad H(\Psi, p, u^*) = \frac{1}{4\eta R^6} \mathbf{w}^T \mathbf{M}^{-1} \mathbf{w}. \quad [\text{S43}]$$

From this, we can write the co-state equations as

$$\dot{p}_X = 0, \quad [\text{S44}]$$

$$\begin{aligned} \dot{p}_R &= -\frac{\partial H}{\partial R} \\ &= -\left\{ -\frac{6H}{R} + \frac{1}{4\eta R^6} 2\mathbf{w}^T \mathbf{M}^{-1} \frac{\partial \mathbf{w}}{\partial R} \right\} \\ &= \frac{6H}{R} - \frac{1}{2\eta R^6} \mathbf{w}^T \mathbf{M}^{-1} \left[ \tilde{\mathbf{v}} + R \frac{\partial \tilde{\mathbf{v}}}{\partial R} \right], \end{aligned} \quad [\text{S45}]$$

where  $\frac{\partial \tilde{\mathbf{v}}}{\partial R} = [p_2 F_R \ p_1 G_X + p_2 G_R]^T$ . Moreover,

$$\begin{aligned} \dot{p}_\nu &= -\frac{\partial H}{\partial \nu} \\ &= -\frac{1}{4\eta R^6} \left\{ 2\mathbf{w}^T \mathbf{M}^{-1} \frac{\partial \mathbf{w}}{\partial \nu} + \mathbf{w}^T \frac{\partial \mathbf{M}^{-1}}{\partial \nu} \mathbf{w} \right\}. \end{aligned} \quad [\text{S46}]$$

183 We find the solution to the optimal transport problem by using CasADi (7). A fourth order Runge-Kutta method is used to  
 184 simulate the dynamics, using time step  $dt = 10^{-3}$ . As the optimal control solutions scale with the viscosity, we set  $\eta = 0.1$  for  
 185 computational convenience, without loss of generality. Since the initialization of the solver affects the optimal control solution  
 186 obtained, we obtain the optimal solution presented in Fig. S3 from initial guesses for the controls: two optimal solutions for the  
 187 symmetric drop and 100 randomized initial values of the control parameters at each time of discretization, uniformly sampled  
 188 in the interval  $[-0.5, 0.5]$ . The mean stress becomes activated during earlier times causing non-monotonic changes in the drop  
 189 size while the gradient component remains close to zero, where during later durations of the transport, the gradient stress  
 190 drives the drop to its prescribed final location, while the shape undergoes significant change from that of a symmetric drop to a  
 191 highly asymmetric one. As expected, in the limit of  $\lambda \rightarrow \infty$  ( $\dot{\nu}, \nu \rightarrow 0$ ), the protocol for the optimal transportation of the drop  
 192 recovers the analytical strategy described for the symmetric drop (Fig. S2).

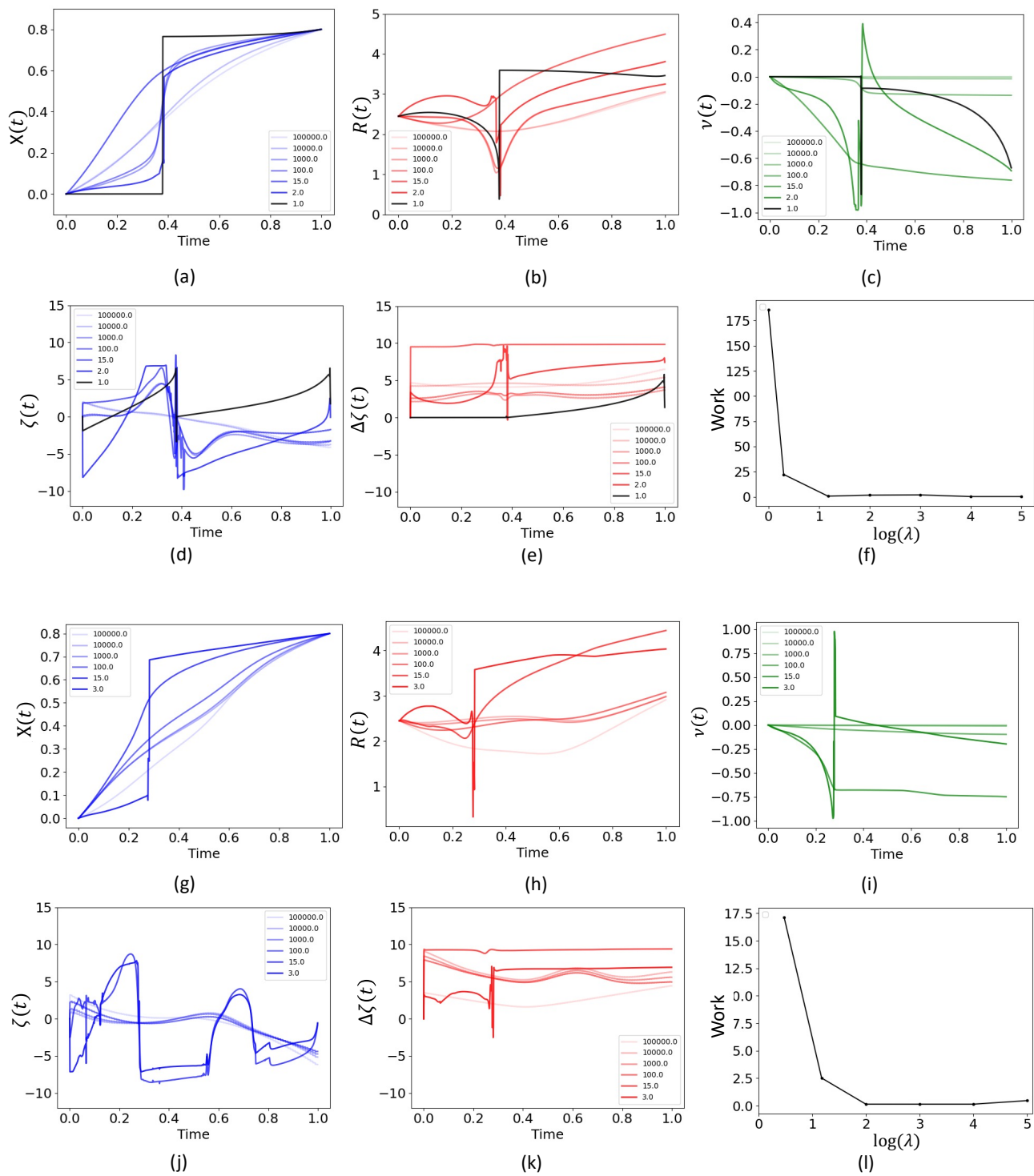


**Fig. S3.** Sensitivity of the optimal control solution to the parameter  $\lambda$  in the equation for asymmetry variable  $\nu$ . The optimal solutions to the drop transport using three dimensional ODE model are obtained via sequentially optimizing while varying  $\lambda$  from  $10^5$  to 1, with the solver at the first iteration initialized by the solution to the optimal transport for the symmetric drop. The optimal control problems were solved in CasADi with time step 0.001. Plots (a)-(f) and (g)-(l) respectively show the solution to the sequential optimization problem starting with the two symmetric solutions from the two dimensional ODE optimal control problem. While the algorithm converges for initialization based on the first symmetric solution when  $\lambda = 1$  corresponding to the asymmetric drop model, it does not for the second solution. We observe that in both cases for smaller values of  $\lambda$ , the drop undergoes rapid changes in size ( $R$ ) and shape ( $\nu$ ), thereby affecting the numerical stability of the optimization.

### 193 3. PDE optimal control

194 The numerical optimization with the PDE constraint is carried out with the evolutionary algorithm CMA-ES (10), using a  
 195 standard Python implementation called pycma (11). The strategy involves solving a large number of forward problems with  
 196 randomly sampled controls and evolving the population to optimize a given cost, which dictates the fitness landscape. We  
 197 discretize and solve the PDE as a forward problem using the finite element method in FEniCS (12, 13). We choose the domain  
 198 to be an interval of length  $L = 8$  with a step size  $dx \approx 0.01$  (resolution  $N = 800$ ). We use a mixed semi-implicit scheme treating  
 199 the nonlinear mobility explicitly using a second order Adams-Bashforth method and the linear stress tensor via Crank-Nicolson.  
 200 Upon choosing  $dt = 5 \times 10^{-3}$  as the integration time-step and a total time  $T = 1$ , we use the following weak form of the PDE,

$$201 \left\langle \left( \frac{h_{n+1} - h_n}{dt} \right), v_1 \right\rangle - \langle q_{n+1/2}, \partial_x v_1 \rangle = 0, \quad [S47]$$

202 where  $q_{n+1/2}$  is the flux evaluated in the middle of the time step and the inner product is  $\langle f, g \rangle = \int dx fg$ . We use second order  
 203 Lagrange elements for our function space basis. To avoid solving a nonlinear equation, we evaluate the flux in a semi-linear  
 204 fashion as

$$205 q_{n+1/2} = \Gamma(h_*) [\partial_x \sigma(h_{n+1/2}) - \Pi'(h_*) \partial_x h_{n+1/2}], \quad [S48]$$

206 where  $h_* = (3h_n - h_{n-1})/2$ ,  $h_{n+1/2} = (h_n + h_{n+1})/2$ . The mobility  $\Gamma$  is regularized to preserve positivity of the solution (given  
 207 a compliant initial condition) as (14, 15)

$$208 \Gamma(h) = \frac{h^4 m(h)}{h^4 + \epsilon m(h)}, \quad m(h) = \frac{h^3}{3\eta}, \quad [S49]$$

with  $\epsilon = 10^{-8}$  and viscosity  $\eta = 0.1$ . The stress  $\sigma$  includes both active and passive (capillary) contributions, with the latter  
 providing numerical stability as well,

$$\sigma(h) = \zeta h + \gamma \mu, \quad [S50]$$

$$\langle \mu, v_2 \rangle + \langle \partial_x h, \partial_x v_2 \rangle = 0. \quad [S51]$$

209 Both test functions,  $v_1$  and  $v_2$  belong to the same function space spanned by second order Lagrange elements. Hence we solve  
 210 for the higher gradient term  $\mu = \partial_x^2 h$  in weak form simultaneously with the continuity equation above. The constant surface  
 211 tension is varied over the range  $\gamma = 0.075 - 2$ . We also include a disjoining pressure  $\Pi(h)$  (16) to fix the contact angle for a  
 212 passive, sessile drop. Along with a precursor film of thickness  $\delta = 10^{-2}$ , we have (17–19)

$$213 \Pi(h) = \frac{\mathcal{A}}{h^3} \left( 1 - \frac{\delta}{h} \right), \quad \Pi'(h) = \frac{\mathcal{A}}{h^5} (4\delta - 3h), \quad [S52]$$

214 where  $\mathcal{A} = 3\gamma\delta^2 \tan^2 \phi_0$ , where  $\phi_0$  is the required contact angle. This expression works better than  $6\gamma\delta^2(1 - \cos \phi_0)$  (19) to  
 215 which it is equivalent for small angles ( $\phi_0 \ll 1$ ). We set  $\phi_0 = \pi/4$  to be the equilibrium contact angle.

216 The boundary conditions are  $\partial_x h = 0$  and  $M\partial_x \sigma = 0$  at the ends of the domain (not the drop). Note, we do not track  
 217 the contact line separately. Mass is naturally conserved within this formulation, which we check numerically as well. We fix  
 218  $\int dx h(x) = 1$  with the integral spanning the whole domain. The initial condition is a symmetric drop centered around the  
 219 origin  $X_0 = 0$  with size  $R_0$ ,

$$220 h(x) = \begin{cases} \delta + \frac{6}{R_0^3} [1 - R_0\delta] \left( \frac{R_0^2}{4} - x^2 \right), & x \in \left[ -\frac{R_0}{2}, \frac{R_0}{2} \right] \\ \delta, & x \notin \left[ -\frac{R_0}{2}, \frac{R_0}{2} \right] \end{cases}. \quad [S53]$$

221 The initial size is fixed by the equilibrium contact angle to be  $R_0 = \sqrt{6/\tan \phi_0} = \sqrt{6}$ . We checked that this initial condition is  
 222 the stable steady state of the passive dynamics if the activity is turned off.

223 The activity  $\zeta$  is taken to be a linear profile in space

$$224 \zeta(x, t) = \zeta_1(t) + \zeta_2(t)x. \quad [S54]$$

Note that this is in the lab frame over the entire domain and not in the drop fixed comoving frame (Eq. 4, main text). While  
 the latter is more convenient to use for the analytical calculations, it is numerically easier to use the entirely equivalent lab  
 fixed parametrization. The mean and gradient activity ( $\zeta_0, \Delta\zeta$ ) and the drop position and size ( $X, R$ ) are computed using

$$\zeta_0 = \frac{1}{R} \int dx \zeta \Theta(h - \delta_c), \quad \Delta\zeta = \zeta_2 R \quad [S55]$$

$$X = \int dx x h, \quad R = \int dx \Theta(h - \delta_c), \quad [S56]$$

225 where  $\Theta(x)$  is the Heaviside step function, and  $\delta_c = 1.1\delta = 1.1 \times 10^{-2}$  is a threshold cutoff to separate the prewetting film  
 226 from the drop. We use a real element with one global degree of freedom to represent  $\zeta_1$  and  $\zeta_2$  and choose to discretize the

control with a coarser time-step than required for a numerically stable integration of the PDE. This keeps the optimization manageable and avoids excessively high-dimensional searches. The control is actuated at  $N_c = 100$  equi-spaced time points, and is linearly interpolated in between.

The cost function  $\mathcal{C} = \mathcal{W} + \mathcal{T} + \mathcal{R}$  involves a time integrated cost from the net dissipated energy ( $\mathcal{W}$ ), a terminal cost ( $\mathcal{T}$ ) and a regularizing term ( $\mathcal{R}$ ), which are given by

$$\mathcal{W} = \int_0^T dt \int dx \frac{h^3}{3\eta} [\partial_x(\sigma - \Pi)]^2, \quad [\text{S57}]$$

$$\mathcal{R} = \frac{\alpha}{N_c} \int_0^T dt [(\partial_t \zeta_1)^2 + (\partial_t \zeta_2)^2], \quad [\text{S58}]$$

$$\mathcal{T} = \mu_X \left( \frac{X(T) - X_T}{X_T} \right)^2 + \mu_R \left( \frac{R(T) - R_T}{R_T} \right)^2. \quad [\text{S59}]$$

We use a trapezoidal rule to discretize the temporal integral in  $\mathcal{W}$  and the spatial integral is computed using standard Gauss quadrature in FEniCS. The temporal regularization term  $\mathcal{R}$  is computed easily by noting that the control is piecewise linear. Note that,  $\mathcal{R} \rightarrow 0$  as  $N_c \rightarrow \infty$  for fixed  $\alpha$  and bounded time derivatives of the activity. The regularization term is used to select smoother controls and is reminiscent of minimal attention control (20). If the total cost is infinite or negative, or if  $h < 0$  at any spatial point at any time, we set it to NaN, forcing CMA-ES to discard the run and reevaluate it for a random sampling of activity. We fix the following parameters,

$$X_0 = 0, \quad R_0 = \sqrt{6}, \quad R_T = 3.0, \quad \eta = 0.1, \quad T = 1, \quad \mu_X = \mu_R = 10^3, \quad [\text{S60}]$$

and vary both the surface tension ( $\gamma = 0.075 - 2$ ) and the terminal drop position ( $X_T = 0.6, 0.8, 1.0, 1.2$ ). For the parameters chosen, both  $X_T = 0.6, 0.8$  correspond to transport tasks for which we have a symmetric solution, while for  $X_T = 1.0, 1.2$ , the symmetric solution doesn't exist. We use multiple initializations for the optimization routine, including the two solutions (one global and one local optimum) we obtain from the symmetric problem (for the parameters where this is unavailable, we use the closest available symmetric solutions using  $X_T = 0.9, R_T = 3$  instead), two independent sets of random activity and a sequential minimization using the best solution obtained. The random activity initializations are uniformly sampled from the interval  $[-\zeta_{\max}/4, \zeta_{\max}/4]$ , where  $\zeta_{\max} = 20$  is the maximum permitted value of the activity to avoid numerical blow-up. We use an initial standard deviation  $\Sigma_{\text{dev}} = 0.2$  for both  $\zeta_1$  and  $\zeta_2$ , along with a default population size of  $N_{\text{pop}} = 19$ . The repeated function calls over the random population are parallelized over  $N_{\text{pop}}$  cores using Python's multiprocessing pool module. The maximum number of iterations is fixed at  $M_{\text{iter}} = 10^6$  and we set the convergence criteria to be

$$\Delta \mathcal{C} \leq \epsilon_{\text{tol}} (C_{\text{median}}^0 - C_{\text{median}}^{\min}), \quad [\text{S61}]$$

where  $\Delta \mathcal{C} = \max(\mathcal{C}) - \min(\mathcal{C})$  is the current spread in the fitness function,  $C_{\text{median}}^0$  is the median of the initial fitness distribution and  $C_{\text{median}}^{\min}$  is the smallest median fitness encountered throughout the optimization trajectory. We choose  $\epsilon_{\text{tol}} = 10^{-4}$ .

#### 4. Minimal dissipation bound

Here we derive the general bound on the minimal amount of energy that must be dissipated if a drop with bounded height achieves a nonzero displacement and size change. Consider a positive and bounded height function  $h(x, t) \geq 0$  with compact nonvanishing support ( $\forall t \in [0, T]$ ) and net unit mass ( $\int dx h = 1$ ) obeying the continuity equation

$$\partial_t h + \partial_x q = 0, \quad q = h \langle u \rangle = \frac{h^3}{3\eta} \partial_x \sigma, \quad [\text{S62}]$$

driven by some arbitrary stress  $\sigma = \sigma(x, t, h, \partial_x h, \dots)$ . Note, we do not specify the rheological constitutive equation for  $\sigma$ , nor the form of the control, so the description is entirely general to bulk stress driven drop motion\*. The net dissipation in the drop is simply

$$\mathcal{W} = \int_0^T dt \int dx h \langle u \rangle \partial_x \sigma = 3\eta \int_0^T dt \int dx \frac{q^2}{h^3}, \quad [\text{S63}]$$

once again irrespective of the constitutive relation for  $\sigma$ . From Eqs. S30 and S31, we know that  $\dot{X} = \int dx q$  and  $\dot{\Delta} = 2 \int dx (x - X)q$ , where the position is  $X = \int dx x h$  and the variance is  $\Delta = \int dx (x - X)^2 h$ . These are all finite as  $h$  is assumed to have compact support at all times. Upon integrating  $\dot{X}$  and using  $X(0) = X_0 = 0$  without loss of generality, we obtain,

$$|X(T)| = \left| \int_{t,x} \left( \frac{q}{h} \right) h \right| \leq \sqrt{\int_{t,x} \frac{q^2}{h^2} \int_{t,x} h^2}, \quad [\text{S64}]$$

where  $\int_{t,x} = \int_0^T dt \int dx$  and we have used the Cauchy-Schwarz inequality. We can now use Hölder's inequality to write

$$\int_{t,x} h^2 \leq \|h\|_{\infty} \int_{t,x} h = T \|h\|_{\infty}, \quad [\text{S65}]$$

\*Drop motion driven by marangoni forces or differential surface wetting are not included in this formalism as they appear as body forces and not stresses in lubrication theory.

265 where  $\|h\|_\infty = \sup_{x,t} h(x,t)$  is the maximum height achieved by the drop at any point along its trajectory (guaranteed to be  
 266 finite by mass conservation and the nonvanishing compact support). Similarly, we can use Eq. S63 and Hölder’s inequality  
 267 again to write

$$268 \int_{t,x} \frac{q^2}{h^2} \leq \|h\|_\infty \int_{t,x} \frac{q^2}{h^3} = \|h\|_\infty \frac{\mathcal{W}}{3\eta}. \quad [\text{S66}]$$

269 Upon combining Eqs. S64-S66 we get

$$270 X(T)^2 \leq \|h\|_\infty^2 \frac{T\mathcal{W}}{3\eta}. \quad [\text{S67}]$$

271 We can perform a similar calculation for the variance  $\Delta$ . This gives (using the Cauchy-Schwarz inequality)

$$272 |\Delta(T) - \Delta(0)| = 2 \left| \int_{t,x} q(x-X) \right| \leq 2 \sqrt{\int_{t,x} \frac{q^2}{h^2} \int_{t,x} h^2(x-X)^2}. \quad [\text{S68}]$$

273 Hölder’s inequality can now be used to simplify the right hand side,

$$274 \int_{t,x} h^2(x-X)^2 \leq \|h\|_\infty \int_0^T dt \Delta(t) = \|h\|_\infty T \langle \Delta \rangle_T, \quad [\text{S69}]$$

275 with  $\langle \Delta \rangle_T$  as the time averaged variance of the drop (also finite). This gives

$$276 |\Delta(T) - \Delta(0)|^2 \leq 4 \frac{T\mathcal{W}}{3\eta} \|h\|_\infty^2 \langle \Delta \rangle_T. \quad [\text{S70}]$$

277 By combining Eqs. S67, S70, we obtain the desired lower bound on the dissipation to be

$$278 \mathcal{W}_{\min} \equiv \frac{3\eta}{2T\|h\|_\infty^2} \left[ X(T)^2 + \frac{|\Delta(T) - \Delta(0)|^2}{4\langle \Delta \rangle_T} \right] \leq \mathcal{W}. \quad [\text{S71}]$$

## 279 5. Supplementary Movies

280 **Movie S1.** Video showing the activity controls  $\{\zeta_0(t), \Delta\zeta(t)\}$ , the state trajectory  $\{X(t), R(t)\}$  and full drop  
 281 profile  $h(x,t)$  corresponding to the optimal solution computed using CMA-ES for a large active capillary  
 282 number ( $\text{Ca}_\zeta = 383.66$ ), or conversely small surface tension ( $\gamma = 0.15$ ). The optimal policy qualitatively  
 283 employs a “gather-move-spread” strategy, though now with complex shape changes of the drop. The drop  
 284 is initialized as a parabola centered at  $X_0 = 0$ , with size  $R_0 = \sqrt{6}$  (equilibrium contact angle  $\phi_{\text{eq}} = \pi/4$ ) with  
 285 terminal position and size fixed to  $X_T = 0.8$  and  $R_T = 3$  respectively. The viscosity ( $\eta = 0.1$ ) and the total time  
 286 ( $T = 1$ ) are fixed as well.

287 **Movie S2.** Video showing the activity controls  $\{\zeta_0(t), \Delta\zeta(t)\}$ , the state trajectory  $\{X(t), R(t)\}$  and full drop  
 288 profile  $h(x,t)$  corresponding to the optimal solution computed from the reduced order ODE model in Eq. 10.  
 289 The activity profile plotted in Fig. 3A is used as the input for the simulation and the surface tension is set  
 290 to a small value ( $\gamma = 0.15$ ) as appropriate for the validity of the ODE model. All other parameters are kept  
 291 the same ( $X_0 = 0$ ,  $R_0 = \sqrt{6}$ ,  $X_T = 0.8$ ,  $R_T = 3$ ,  $\eta = 0.1$ ,  $T = 1$ ) The drop trajectory is qualitatively similar to the  
 292 full optimal solution (shown in Movie S1 and Fig. 4A) but not quantitatively accurate, for instance, the final  
 293 drop position and size only reach about half the values set by the task.

294 **Movie S3.** Video showing the activity controls  $\{\zeta_0(t), \Delta\zeta(t)\}$ , the state trajectory  $\{X(t), R(t)\}$  and full drop  
 295 profile  $h(x,t)$  corresponding to the optimal solution computed using CMA-ES for a small active capillary  
 296 number ( $\text{Ca}_\zeta = 30.91$ ), or conversely small surface tension ( $\gamma = 2$ ). The optimal policy is now quite different,  
 297 with futile size oscillations that initially dissipate energy without translation and a final activity burst that  
 298 advances the drop at the end of the policy. The drop is initialized as a parabola centered at  $X_0 = 0$ , with size  
 299  $R_0 = \sqrt{6}$  (equilibrium contact angle  $\phi_{\text{eq}} = \pi/4$ ) and the terminal position and size are  $X_T = 0.8$  and  $R_T = 3$   
 300 respectively. The viscosity ( $\eta = 0.1$ ) and the total time ( $T = 1$ ) are fixed as well.

## 301 References

- 302 1. RW Brockett, *Finite dimensional linear systems.* (SIAM), (2015).
- 303 2. R Hermann, A Krener, Nonlinear controllability and observability. *IEEE Transactions on automatic control* **22**, 728–740  
 304 (1977).
- 305 3. RS Strichartz, Sub-riemannian geometry. *J. Differ. Geom.* **24**, 221–263 (1986).
- 306 4. A Agrachev, D Barilari, U Boscain, *A comprehensive introduction to sub-Riemannian geometry.* (Cambridge University  
 307 Press) Vol. 181, (2019).

- 308 5. V Jurdjevic, *Geometric control theory*. (Cambridge university press), (1997).
- 309 6. L Pontryagin, *Mathematical Theory of Optimal Processes*. (CRC Press), (1987).
- 310 7. JA Andersson, J Gillis, G Horn, JB Rawlings, M Diehl, Casadi: a software framework for nonlinear optimization and  
311 optimal control. *Math. Program. Comput.* **11**, 1–36 (2019).
- 312 8. P Curie, Sur la symétrie dans les phénomènes physiques, symétrie d’un champ électrique et d’un champ magnétique. *J. de*  
313 *physique théorique et appliquée* **3**, 393–415 (1894).
- 314 9. WR Inc., Mathematica, Version 12.0 (2019) Champaign, IL.
- 315 10. N Hansen, *The CMA Evolution Strategy: A Comparing Review*, eds. JA Lozano, P Larrañaga, I Inza, E Bengoetxea.  
316 (Springer Berlin Heidelberg, Berlin, Heidelberg), pp. 75–102 (2006).
- 317 11. N Hansen, Y Akimoto, P Baudis, CMA-ES/pycma on Github (Zenodo, DOI:10.5281/zenodo.2559634) (2019).
- 318 12. A Logg, KA Mardal, G Wells, *Automated solution of differential equations by the finite element method: The FEniCS book*.  
319 (Springer Science & Business Media) Vol. 84, (2012).
- 320 13. M Alnæs, et al., The fenics project version 1.5. *Arch. Numer. Softw.* **3** (2015).
- 321 14. AL Bertozzi, M Pugh, The lubrication approximation for thin viscous films: the moving contact line with a porous  
322 media cut-off of van der waals interactions. *Nonlinearity* **7**, 1535 (1994).
- 323 15. L Zhornitskaya, AL Bertozzi, Positivity-preserving numerical schemes for lubrication-type equations. *SIAM J. on Numer.*  
324 *Analysis* **37**, 523–555 (1999).
- 325 16. PG De Gennes, Wetting: statics and dynamics. *Rev. modern physics* **57**, 827 (1985).
- 326 17. F Brochard-Wyart, JM Di Meglio, D Quéré, PG De Gennes, Spreading of nonvolatile liquids in a continuum picture.  
327 *Langmuir* **7**, 335–338 (1991).
- 328 18. PG De Gennes, F Brochard-Wyart, D Quéré, *Capillarity and wetting phenomena: drops, bubbles, pearls, waves*. (Springer  
329 Science & Business Media), (2013).
- 330 19. AA Pahlavan, L Cueto-Felgueroso, AE Hosoi, GH McKinley, R Juanes, Thin films in partial wetting: Stability, dewetting  
331 and coarsening. *J. Fluid Mech.* **845**, 642–681 (2018).
- 332 20. RW Brockett, Minimum attention control in *Proceedings of the 36th IEEE Conference on Decision and Control*. (IEEE),  
333 Vol. 3, pp. 2628–2632 (1997).